

Styles of slope instability on a Quaternary sub-arctic continental margin: The northwest flank of the Storegga Slide

Song Jing^{a,c}, Tiago Alves^{a,*}, Kamal'deen O. Omosanya^b

^a 3D Seismic Laboratory, School of Earth and Environmental Sciences, Cardiff University, Main Building, Park Place, Cardiff, CF10 3AT, United Kingdom

^b Department of Geoscience and Petroleum, Norwegian University of Science and Technology, Trondheim

^c CAS Key Laboratory of Ocean and Marginal Sea Geology, South China Sea Institute of Oceanology, Chinese Academy of Sciences, Guangzhou 510301, China

ARTICLE INFO

Editor: Michele Rebesco

Keywords:

Norwegian margin
Storegga Slide
Pleistocene landslides
Fluid flow
Ooze evacuation

ABSTRACT

Submarine landslides are widely recognised around the Northeast Atlantic margin, some of which forming vast slide complexes. On the mid-Norwegian margin, the Storegga Slide complex has been active since the early Pleistocene, first as a regional event (Slide W) at 1.7 Ma, and later culminating in the Storegga Slide *sensu stricto* at 8.2 ka. By interpreting high-quality seismic data, this work investigates slope instability styles, and their geneses, on the northwest flank of the Storegga Slide complex. Seismic and borehole data prove: i) the presence of two new landslides formed prior to Slide W, ii) that mass-transport complexes occurred during the evacuation of sediment oozes, iii) the existence of a series of cracks on the seafloor, denoting modern slope instability. Fluid accumulation in glacial-marine deposits was a primary factor promoting early instability; fluid pipes increase in number below the oldest landslide deposits, with most pipes terminating at their glide planes. Furthermore, mathematical models show that vertically stacked intervals with weak layers, and older landslide deposits, are able to promote further instability. This work thus suggests episodic fluid flow as the primary factor promoting long-term instability near the Storegga Slide complex. As a corollary, we reveal the stability of the continental slope to still be precarious, at present, on the northwest flank of the Storegga Slide.

1. Introduction

Submarine landslides comprise one of the most important geohazards in nature, being able to trigger recurrent episodes of seafloor deformation, sediment remobilisation and, in extreme cases, catastrophic tsunamis (Harbitz et al., 2006; Hühnerbach and Masson, 2004; Kawamura et al., 2012; Locat and Lee, 2002; Pakoksung et al., 2019; Schulten et al., 2019; Sun et al., 2022). The Storegga Slide, the best known submarine landslide in Northwest Europe, evacuated around 3000 km³ of strata since ~8.2 ka and affected as much as 95,000 km² of Norway's continental margin (Bugge et al., 1988; Hafliðason et al., 2005) (Fig. 1). Several pre-Holocene mass-transport complexes (MTCs) were triggered before the Storegga Slide, from Slide W occurring prior to 1.7 Ma, to the Tampen Slide dated at ~0.15 Ma (Solheim et al., 2005). Such MTCs show instability to be recurrent on Norway's continental margin (Elger et al., 2018; Rise et al., 2005), particularly within a broad area named in the literature as the *Storegga Slide complex* (e.g., Bryn et al., 2003; Solheim et al., 2005; Hill et al., 2004). A record-breaking 20-m tsunami is believed to have affected the Scottish, Norwegian and

Faroese coasts when the largest of these recurrent events occurred at 8.2 ka (Bondevik, 2019; Bondevik et al., 2012; Romundset and Bondevik, 2011).

Three (3) Quaternary MTCs have been previously identified along the northwest flank of the Storegga Slide and named R, S and W, from the youngest to the oldest, by Hafliðason et al. (2004). Significantly, the oldest of these slides, Slide W, comprises ooze craters (also named as 'evacuation structures') containing multiple slide blocks and ooze mounds (Riis et al., 2005; Solheim et al., 2005). Another early Quaternary MTC – 'Slide Y' in Lawrence and Cartwright (2009) – was also recognised around the headwall region of the Storegga Slide, but its initiation and further development are not fully understood. It is thus crucial to improve our understanding about distinct aspects of slope failure around the Storegga Slide, investigating the geological conditions controlling long-term slope instability on continental slopes (Fig. 1a). Moreover, information is still scarce on the northwest flank of the latter slide, and any new findings will be important to predict future geological hazards on continental margins.

The sequence of landslides generated on the northwest flank of the

* Corresponding author.

E-mail address: AlvesT@cardiff.ac.uk (T. Alves).

<https://doi.org/10.1016/j.margeo.2022.106933>

Received 24 January 2022; Received in revised form 21 October 2022; Accepted 25 October 2022

Available online 1 November 2022

0025-3227/© 2022 The Authors. Published by Elsevier B.V. This is an open access article under the CC BY license (<http://creativecommons.org/licenses/by/4.0/>).

Storegga Slide is mapped in this work based on high-resolution 3D seismic and borehole data (Fig. 1b and c). Seismic attributes such as seismic amplitude and variance are used to reveal features associated with local fluid accumulation, older landslides and evacuation structures (ooze craters). By focusing on the chronology of Quaternary submarine landslides around the Storegga Slide, and resulting structures affecting the modern seafloor, we address the following research questions:

- What features precede the failure of the first regional-scale landslide near the Storegga Slide?
- How were ooze evacuation structures (craters) developed in relation to regional-scale landslides, ascending oozes, and infilling MTCs?
- Which key seismic-scale features indicate instability on the modern continental slope of Mid Norway?

2. Geological setting

2.1. Lithostratigraphy

Cretaceous-Paleocene strata were deposited on the mid-Norwegian margin before the breakup of the NE Atlantic. This pre-breakup phase of deposition ended with the Tang Formation, which comprises the oldest sediments imaged in the study area (Jongepier et al., 1996; Kjøberg et al., 2017) (Figs. 2 and 3). Upper Cretaceous-Paleocene strata are thus composed of sandstones, mudstones and limestones (Dalland, 1988; Knaust, 2009; Lien, 2005). Magma intruded Cretaceous-Paleocene strata during and soon after continental breakup, forming large hydrothermal vent complexes (Berndt et al., 2000; Kjøberg et al., 2017; Omosanya et al., 2018; Planke et al., 2005; Roelofse et al., 2021; Skogseid et al., 1992).

The post-rift Brygge Formation (Early Eocene-Early Miocene; Eidvin et al., 2007) contains significant volumes of biogenic ooze, which alternate with intervals of sandstone, siltstone, limestone and marl (Dalland, 1988; Eldholm et al., 1987). The unit is divided into the upper Brygge Formation, with a relatively low density of 1.4 g/cm³, and the lower Brygge Formation with a density of 1.8 g/cm³ (Fig. 3). The entire Brygge Formation was deformed above hydrothermal vents by

polygonal and radial faults (Fig. 2) (Song et al., 2020).

The Kai Formation accumulated from the Middle Miocene to the Pliocene in deep waters (Hjelstuen et al., 1999; Swiecicki et al., 1998). Calcareous and siliceous oozes with a density of 1.5 g/cm³ predominate in this unit (Ireland et al., 2011; Neagu et al., 2010) (Fig. 3). Some minor, localised unconformities mark discrete episodes of uplift on the South Modgunn Arch (Song et al., 2020). Furthermore, an Opal A/CT diagenetic boundary occurs together with polygonal faults in the study area (Brekke, 2000; Davies and Cartwright, 2002; Neagu et al., 2010) (Fig. 2b).

The lower Pleistocene Naust Formation was deposited synchronously with the onset the Northern Hemisphere glaciations. It comprises alternating glacial and marine deposits (Forsberg and Locat, 2005; Hjelstuen et al., 2004) with a relatively high density of 1.85 g/cm³ (Dalland, 1988; Song et al., 2020) (Fig. 3).

Clay-rich intervals divide the Naust Formation into five (5) well-dated packages, from the earliest Naust W unit deposited before 1.7 Ma to the Naust O unit accumulated after 200 ka (Berg et al., 2005). The Naust Formation reveals important progradation of sediment during ice-sheet advance (Berg et al., 2005; Newton and Huuse, 2017; Rise et al., 2010; Rise et al., 2005; Rydningen et al., 2016). Multiple regional landslides accompanied sediment progradation of sediment in the Naust Formation, starting with the lower Pleistocene Slide W, up to the Storegga Slide formed at ~8.2 ka.

2.2. Factors preconditioning slope instability

On the mid-Norwegian margin, excess pore pressure has been considered as the dominant preconditioning factor for slope instability (Solheim et al., 2005). Near the Storegga Slide, potential phenomena creating excess pore pressure include the dehydration of ooze deposits (Awadalkarim et al., 2014; Chand et al., 2011; Ulaub et al., 2018), the dissociation of gas hydrates below the seafloor (Elger et al., 2018; Hustoft et al., 2007; Xu and Germanovich, 2006), and episodes of rapid sedimentation associated with glacial-interglacial climatic cycles (Hustoft et al., 2009; Leynaud et al., 2007).

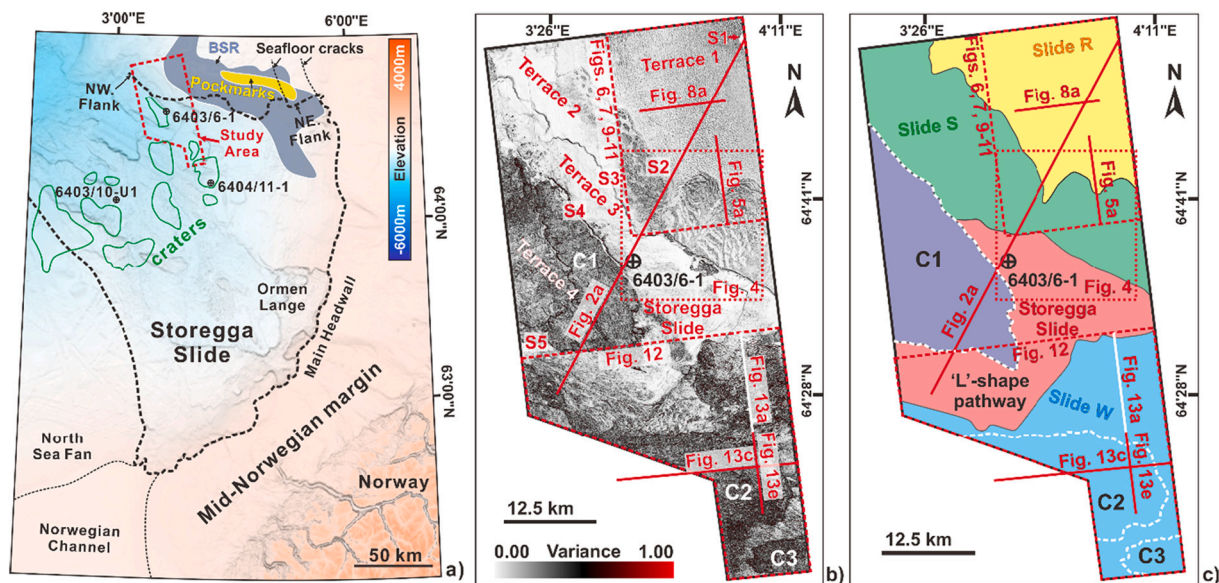


Fig. 1. a) Location of study area on the northwest flank of the Storegga Slide, mid-Norwegian margin, highlighting the distribution of pockmark fields, BSRs (Bünz et al., 2003), craters/evacuation structures (Lawrence and Cartwright, 2010; Riis et al., 2005) and seafloor cracks (Mienert et al., 2010; Reiche et al., 2011). Maps are modified from GEBCO Compilation Group (2020). b) Variance map 50 ms twt above the basal glide plane showing main features in multiple submarine landslides. c) Relationship amongst multiple Quaternary slides in the study area, including craters, Slides W, S, R, and the Storegga Slide (Solheim et al., 2005). C1–C3: craters 1–3 (Omosanya et al., 2022).

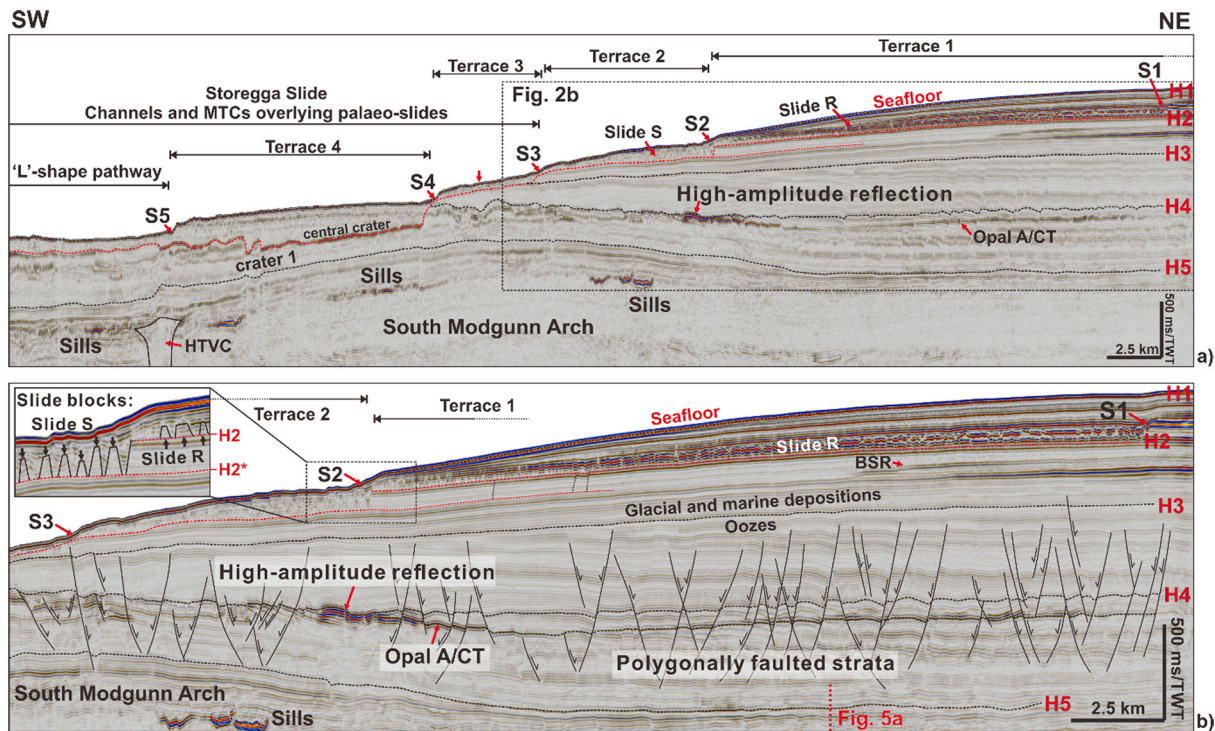


Fig. 2. Seismic profiles of the study area showing the distribution of multiple slides above the South Modgunn Arch. Location of seismic profile shown in Fig. 1. Horizon 1: seafloor; Horizons 2 and 2*: basal glide plane of multiple slides; Horizon 3: top Kai Formation; Horizon 4: top Brygge Formation; Horizon 5: top Tare Formation. The Opal A/CT transition zone does not follow the geometry of any particular seismic reflection but is, nonetheless, locally uplifted around the South Modgunn Arch.

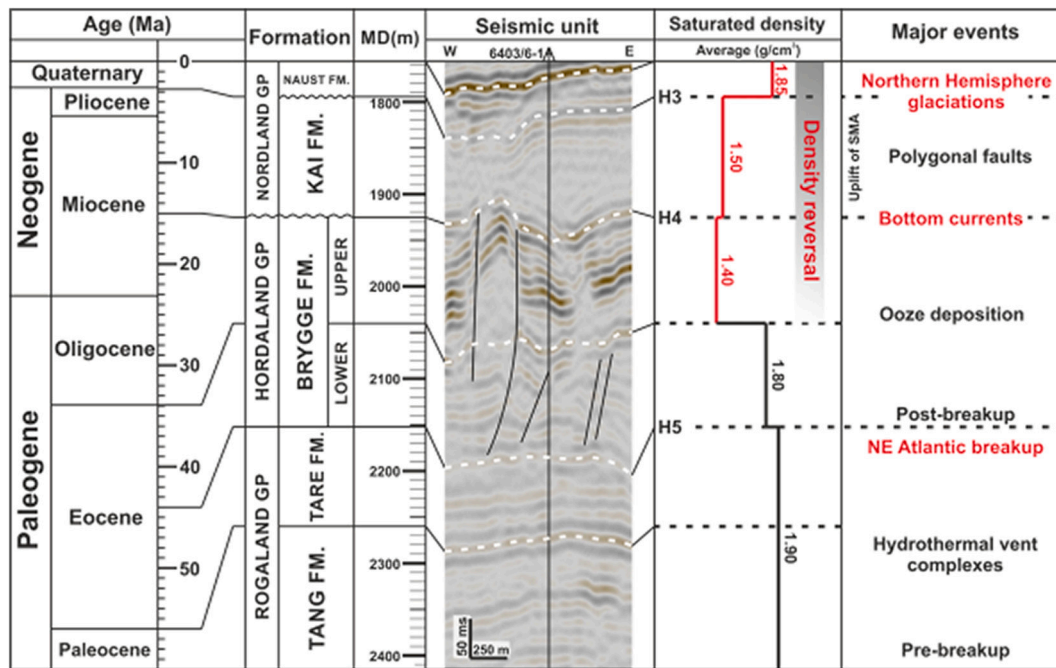


Fig. 3. Summary panel correlating seismic data with the main seismic-stratigraphic units in the South Modgunn Arch. Interpreted key seismic horizons include Horizon 3 – top Kai Formation, Horizon 4 – top Brygge Formation; Horizon 5 – top Tare Formation. Seismic units, local stratigraphic and density data are modified from Song et al. (2020), Roelofse et al. (2021) and Omosanya et al. (2022).

2.2.1. Gas-hydrate dissociation

On the mid-Norwegian margin, episodic release of excess pore pressure is inferred near pipes and bottom-simulating reflectors (BSRs), which mark the base of the gas-hydrate stability zone (GHSZ) (Berndt

et al., 2004; Büinz et al., 2003). During the Quaternary, the flow of warm-water currents, and glaciation-related eustatic sea level, controlled the depth and extent of the GHSZ within which gas hydrates are stable (Mienert et al., 2005). Based on the isotope composition of benthic

foraminifera, a rapid increase of bottom-water temperature has occurred on the mid-Norwegian margin since the end of Younger Dryas (Berstad et al., 2003), promoting the dissociation of gas hydrates and building up excess pore pressure around the headwall of the Storegga Slide (Sultan et al., 2004; Xu and Germanovich, 2006).

2.2.2. Glacial-interglacial cycles and their effect on slope sedimentation

Similarly to other landslides on high-latitude continental margins, interbedded glacial and marine deposits such as those in the Naust Formation contribute to a weakening of slope strata and the accumulation of excess pore pressure in glacial intervals, later remobilising the more sensitive marine clays (Leynaud et al., 2007). Together with rapid sediment deposition and loading, gas hydrate dissociation, tectonic tilting and the dewatering of sediment oozes in the Brygge and Kai formations have all contributed to the migration of fluid to the shallower Naust Formation via hydrothermal vent complexes, polygonal faults and fluid pipes, further increasing pore overpressure and promoting slope instability (Gay and Berndt, 2007; Hustoft et al., 2007; Roelofse et al., 2021).

2.2.3. Density reversal in buried strata

The density of strata normally increases during diagenesis and early sediment burial in tandem with a decrease in porosity (Terzaghi, 1925). However, a reversal in the density of near-seafloor sediment is recognised where high-density glacial/marine deposits overlie low-density marine oozes (Riis et al., 2005; Vogt, 1997). During the failure of Slide W, in the early Pleistocene, low-density oozes were remobilised as ooze mounds and ascended towards the surface of crater-filling MTCs (Lawrence and Cartwright, 2010; Riis et al., 2005; Omosanya et al., 2022). In contrast with submarine landslides, which have headwalls, sidewalls and scarps within a failed region of the slope (Li et al., 2017; Shanmugam, 2021), these ooze craters are recognised as local depressions (Riis et al., 2005).

3. Data and methods

3.1. Dataset

This work uses high resolution 3D seismic and well data from the northwest flank of the Storegga Slide (Fig. 1). The 3D seismic volume images several sidewall and headwall scarps of Quaternary landslides, including Slides W, S, R, and the Storegga Slide proper (Bryn et al., 2003; Micallef et al., 2016; Reiche et al., 2011; Solheim et al., 2005) (Fig. 1b and c). The seismic data were processed with a 12.5 m bin size and their vertical resolution approaches 8 m in the interval of interest (Roelofse et al., 2021).

The 3D seismic volume was interpreted on Schlumberger's Petrel®. Local structures were investigated by computing variance and seismic amplitude maps, complemented by their detailed interpretation on vertical seismic sections. Root Mean Square (RMS) amplitude maps, seismic variance volumes and slices, were used to image the distribution of strata, terraces and relevant internal features in MTCs. In contrast to seismic amplitude, which reflects changes in acoustic impedance, variance can convert a volume of continuity (normal seismic reflections) into a volume of discontinuity, i.e. faults and other boundaries (Brown, 2011). In addition, we adopted the method in Alves (2012) and Roelofse et al. (2021) to plot the relative distribution of MTCs and fluid pipes. The method proposes the counting of the number of seismic reflectors above and below key seismic reflections where geological features are recorded.

The seismic horizons interpreted in this work were tied to wireline and lithological data from well 6403/6-1, which is located in the study area (Fig. 1). In addition to well 6403/6-1, several other exploration wells have been drilled in the region affected by the Storegga Slide complex, providing detailed lithostratigraphic and wireline information (Fig. 1a). To illustrate the styles of slope instability in the study area,

eight (8) seismic horizons were interpreted and mapped: the modern seafloor (H1), the basal glide plane of regional slides (H2), the boundary between the Naust and Kai formations (H3) and other key reflections recording local slides and pipes (Fig. 2). The relative distribution of slope failures between these seismic reflections is described below.

3.2. Evolution models of slope instability

In this study, a computational fluid dynamics (CFD) approach is used in Ansys® Fluent® for the numerical simulation of slide blocks and associated glide-plane propagation. Due to the relative location of the study area on the northwest flank of the Storegga Slide, the numerical simulation focused on understanding the initial phases of slope failure. The soft, clay rich Naust formation was modelled as a non-Newtonian fluid. In seismic data, undercutting processes were revealed by the presence of multiple scarps on a slope that records, for almost its entire length, a gradient $<1^\circ$ underneath Slides S and R. Thus, the models in this paper considered the existence of weak layers and scarps as important features controlling the style and development of submarine landslides in the study area.

During our CFD analysis, strata (a non-newtonian fluid) were modelled as an Eulerian material. Momentum and mass transfer processes were modelled by solving the Navier-Stokes' and additional transport equations. In Fluent®, the models were set as 2D planar models with laminar flow. More detail on the modelling completed in this work is provided in Supplementary File 1.

4. Mapping and characterisation of slope instability styles

4.1. Slope undercutting and slide-block spreading

Submarine spreading around the headwall of the Storegga Slide is recorded as an interval with slide blocks (Kvalstad et al., 2005). This gravity-driven sliding process was triggered by a loss of lateral support on the continental slope (undercutting), overloading, and build-up of pore pressure (Baeten et al., 2013). Above a glide plane, the tops of the less deformed slide blocks are oriented perpendicular to their direction of movement (Micallef et al., 2016).

In the study area, at least two intervals with slide blocks are associated with Slides S and R and draped by a contourite interval (Fig. 4a–c). Beneath the seafloor in Terrace 2, the interior of the slide blocks is increasingly coherent downslope from scarp 2 (Fig. 4f). These blocks were detached above multiple weak layers - their glide planes follow different weak layers on both sides of 'cross points' in Fig. 4c and become larger in a downslope direction (marked blocks in Fig. 4f), having been further disrupted to form debrites (Fig. 4a). Above the deeper glide plane (Horizon H2), most blocks shown on the variance time slices are arcuate (Fig. 4f). These blocks are spaced 1000–2000 m apart and up to 80 ms high. The length (L) of the blocks varies from 800 m to 3600 m, and their width (W) ranges from 200 m to 600 m.

Due to differential compaction, the strata above the blocks developed folds that generate seafloor relief (local folds in Fig. 4d). Some of these positive features also accompany areas with high variance, particularly where faults propagate to the seafloor from the tops and flanks of the slide blocks (Fig. 4a and e). Several small-scale slides are sourced from scarp S2 (Fig. 4e). Beneath an exposed glide plane, there are faults linking this glide plane to slide blocks underneath (Fig. 4b).

Slope undercutting is revealed by the multiple scarps interpreted in seismic data (Fig. 4). In parallel, the gentle glide plane at horizon H2 matches the level of stratified beds on the intact upper slope (Fig. 5a), suggesting the presence of weak layers at the broader, regional scale, on the mid-Norwegian margin (L'Heureux et al., 2012). Geochronology and physical property data correlate these weak layers with the presence of marine clays, deposited during interglacial stages, with high clay content and lower shear strengths. In fact, clay content increases from 30 to 40% in glacial deposits to 50–60% in marine clay, while shear strength

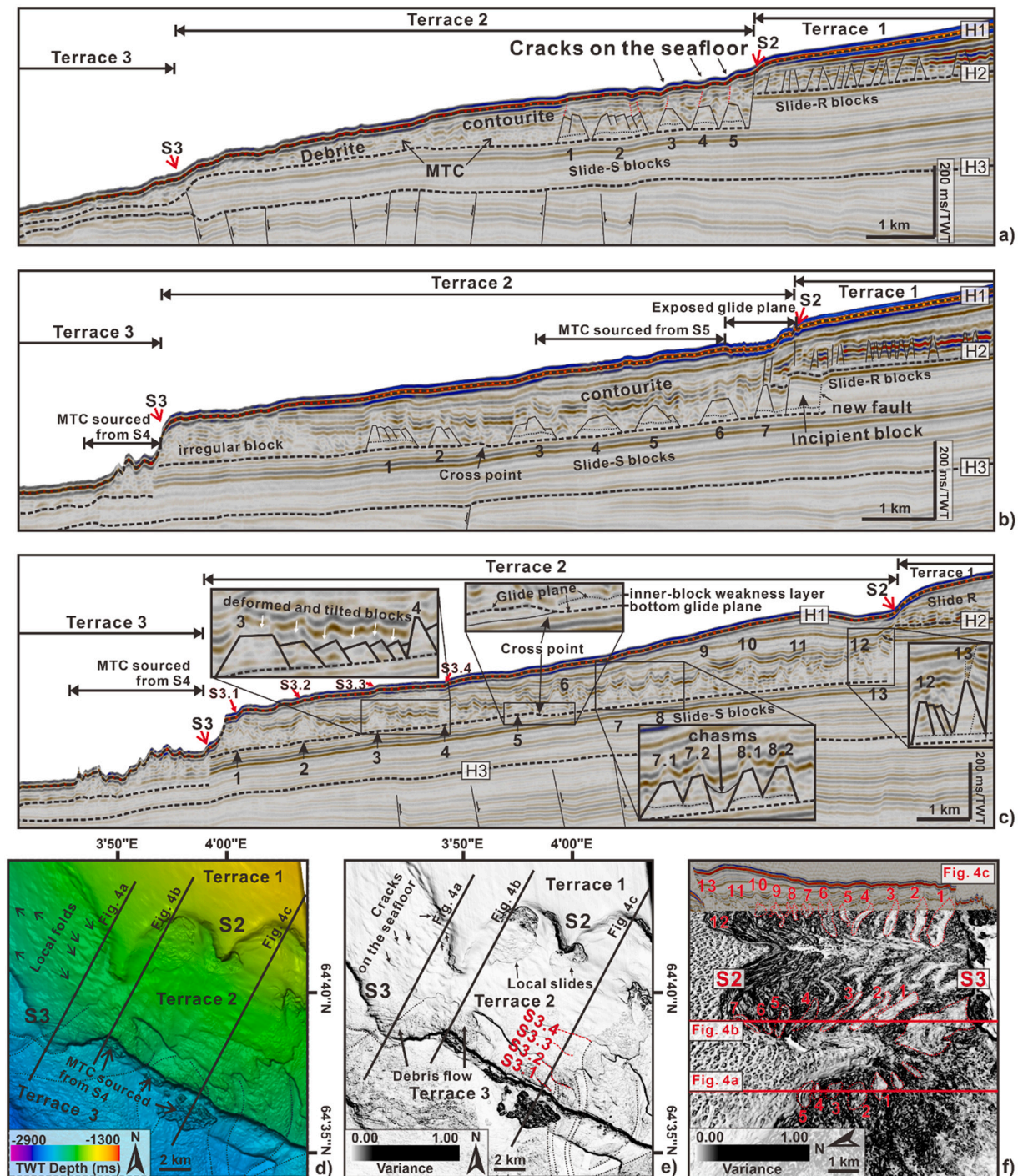


Fig. 4. a–c) Selected seismic profiles across Terrace 2. Slide blocks on Terrace 2 are draped by a thin interval of contourites, and differential compaction in these same contourite deposits generated small-scale folds above blocks. Due to a loss in lateral support (undercutting) on the continental slope when the Storegga Slide occurred (~8.2 ka), slope failure was resumed along scarps and folds generating local MTCs, secondary scarps (S3.1–S3.4) and faults. d, e) TWT structure and variance maps of the seafloor (H1). Local folds above slide blocks are observed as local seafloor highs (see Fig. 4d). Faults on folds are high-variance features in Fig. 4e. f) 3D view of a variance slide extracted 50 ms above the bottom glide plane of the slide blocks (Horizon 2). The locations of profiles a–c are shown by the red lines in Fig. 4f. Slide blocks on Terraces 1 and 2 are separated by scarp S2. (For interpretation of the references to colour in this figure legend, the reader is referred to the web version of this article.)

decreases by around 20% (Bryn et al., 2003; L’Heureux et al., 2013). The blocky detached intervals above represent stiffer glacial deposits with relatively lower clay content (Berg et al., 2005; Solheim et al., 2005).

4.2. Slope instability features below Slide W

In the shallower part of the study area, a local mass-wasting deposit (Slide X) pre-dating Slide W is revealed as a series of high-amplitude detached blocks and associated cracks (e.g., blocks 1–3 in Figs. 5b and 6c). Formed between Horizons B and E, the thickness of this blocky

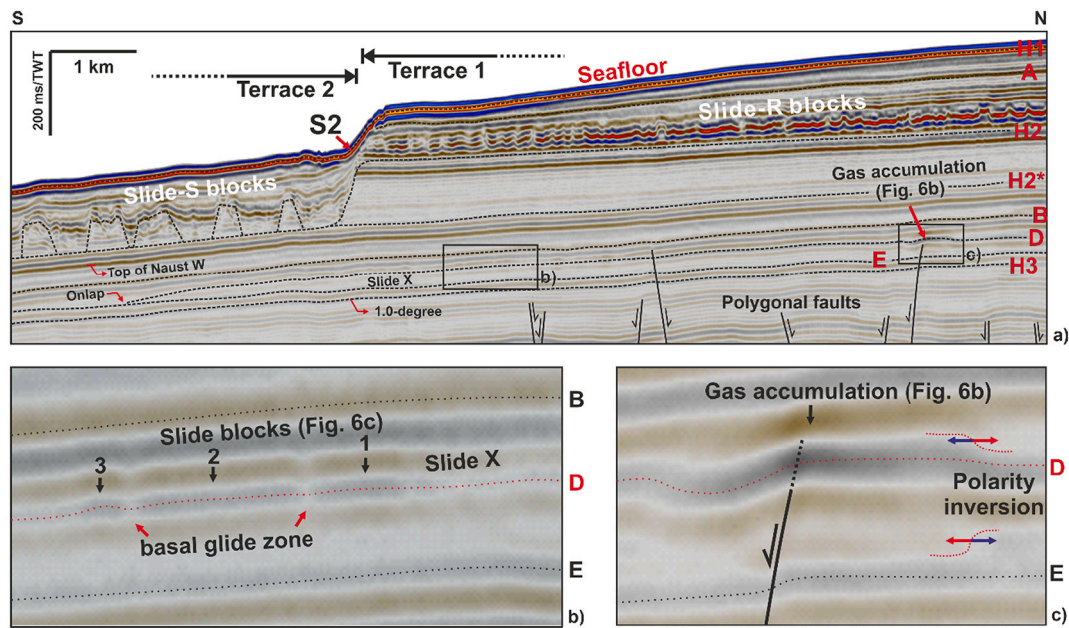


Fig. 5. a) Interpreted north-south seismic profile across Terraces 1 and 2. Location of seismic profile shown in Fig. 1. b) Slide blocks in Slide X are detached on a steeper slope reaching 1.0 degrees in gradient. c) A reversal in seismic polarity is observed laterally close to tip of a polygonal fault and is found to comprise the gas accumulation features highlighted in Fig. 6b.

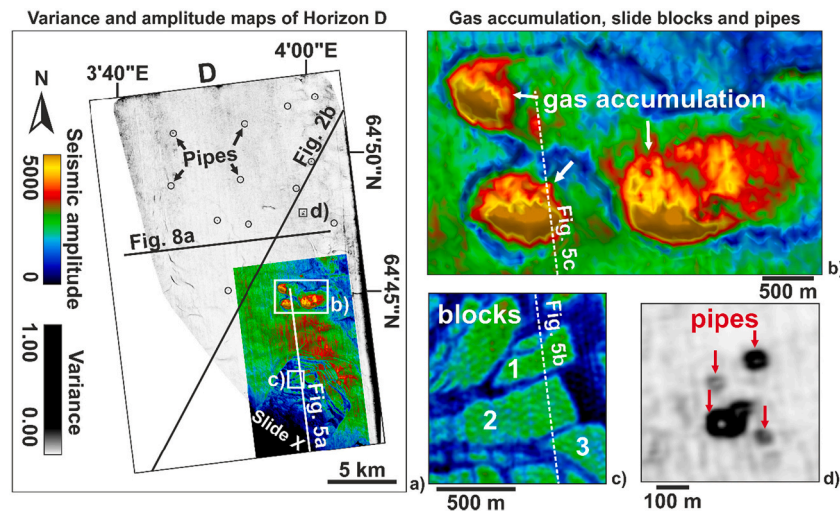


Fig. 6. a) Variance map overlain by the amplitude map of Horizon D, a negative-amplitude reflection beneath Horizon B. b) Gas accumulation features, and c) slide blocks shown as local high-amplitude features. d) Fluid pipes observed at the level of Horizon D.

landslide reaches 40 ms two-way time (twt), or approximately 28 m, and its width is about 6 km. It spans an area of 25 km² and shows a total volume of 0.63 km³ (Figs. 5b and 6a). Blocks in Slide X have varying widths, from 50 to 500 m. Their strike is also variable being, in places, perpendicular to the strike of Slide X's headwall, or rotated by ~45° relative to this same feature (Fig. 6c). At the level of Horizon E, a negative-amplitude reflection immediately below Horizon D, slide blocks become gradually inconspicuous (Fig. 5b). The variance map of Horizon E, the first negative-amplitude seismic reflection above the Kai Formation, shows series of faults and pipes, but no slide blocks or other slide-related features (Fig. 7a).

Behind the headwall of the Slide X, and several slide-related faults, three elliptical areas with positive amplitude are observed in Horizon D (Figs. 5c and 6b). These local elliptical features show major axes that are 1–3 km long, and minor axes about 1 km long (Fig. 6b). Below them, a normal fault is observed to grow out of polygonal faults in the Kai

Formation (Fig. 5c). These local amplitude highs are interpreted to represent gas pockets, or 'flags', particularly where polarity inversion is observed along continuous seismic reflectors (Fig. 5c).

Horizons B and C were also mapped between Horizon D and the 'top of Naust W' surface (Fig. 8a and b). Groups of en echelon and partly connected cracks are observed on seismic amplitude maps (see the green lineations in Fig. 9). These cracks are ~4 km long and 40 m wide, with no apparent offset, and are associated with pipe structures in seismic data (Fig. 8d). Downslope from these cracks, two local ridges show positive relief and a width of approximately 40 m (Fig. 9); they follow the same strike of cracks further upslope (see the local positive structures in Fig. 9c). All the cracks and ridges occur in a specific interval between Horizon D and the top of Naust W.

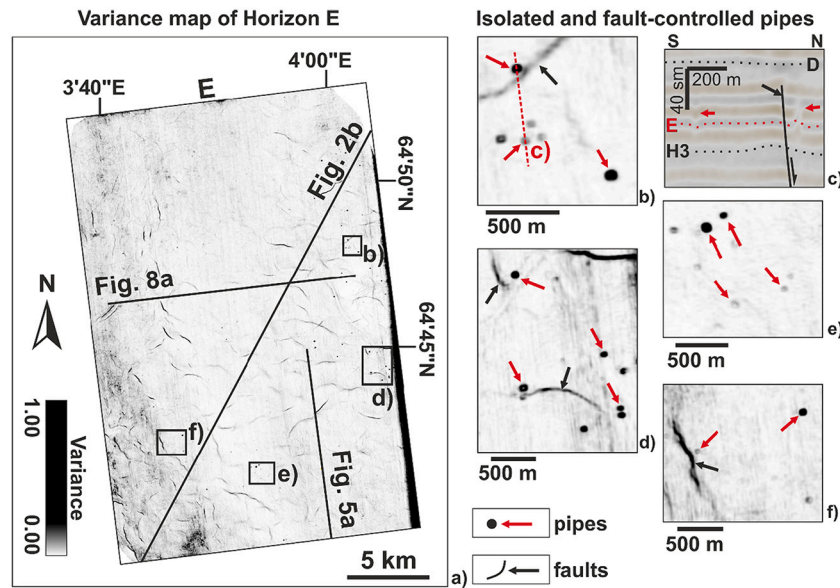


Fig. 7. a) Variance map of Horizon E, a negative seismic reflector above Top Kai (Horizon 3). b–f) Regional pipes observed close to faults as relatively isolated features. Two examples of pipes, including isolated pipes and the some formed close to faults, are marked by the red arrows in (b) and (c). (For interpretation of the references to colour in this figure legend, the reader is referred to the web version of this article.)

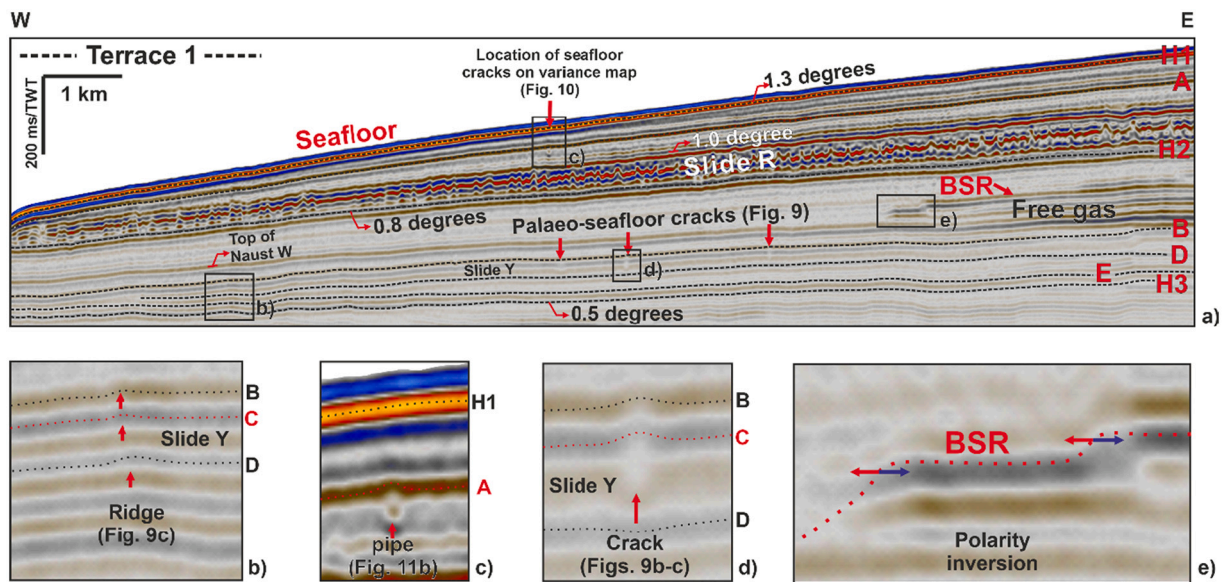


Fig. 8. a) Interpreted west-east seismic profile across Terrace 1. Location of seismic profile is shown in Fig. 1. b) One of ridges observed on the lower part of the slope (see Fig. 9c). c) Palaeo-pipes are observed beneath the modern seafloor. d) En-echelon palaeo-seafloor crack imaged in Fig. 9b. e) Free gas accumulated beneath a BSR, leading to a polarity reversal in amplitude. The average gradient of Terrace 1 increases from 0.5 degrees at the top of the Kai Formation (Horizon 3) to 1.3 degrees on the modern seafloor (Horizon 1).

4.3. Slope instability features on the modern seafloor

Between scarps 1 and 2, originally formed during Slides R and S (Terrace 1 in Fig. 8), the variance maps of the modern seafloor (Horizon 1) and the seismic reflection immediately below (Horizon A) reveal cracks over fluid-related pipes (Figs. 10b and 11b). On the modern seafloor, these en echelon cracks are observed as northwest-striking fractures that are about 800 m long and 80 m wide (Fig. 10b). At the level of Horizon A, a positive-amplitude reflection ~40 ms twt (about 28 m) below the seafloor, several pipes are recognised as high-variance features with circular shapes (Fig. 11). Their average width is about 60 m and their depth is about 20 ms twt (about 14 m) (Fig. 8c). In parallel, at least three small east-west, curvilinear features are observed in

Horizon A with a length of 2–8 km and a width of 200–400 m (Fig. 11a). Similar linear structures are also observed along the mid-Norwegian shelf and were identified as the iceberg ploughmarks carved on the seafloor following major pulses of iceberg discharge from the Fennoscandian Ice Sheet during the middle and late Quaternary (Dowdeswell et al., 2007; Montelli et al., 2018).

Since the last landslide event associated with the Storegga Slide, long-term instability has caused local slumping, debris channels, locally deformed strata, and near-seafloor fractures (Hafliðason et al., 2005; Hafliðason et al., 2004; Micallef et al., 2016; Mienert et al., 2010). Along the northeast flank of the Storegga Slide (Nyegga area) and the outer shelf edge to the north of the main Storegga Slide headwall, series of en echelon cracks are observed on the modern seafloor (Mienert et al.,

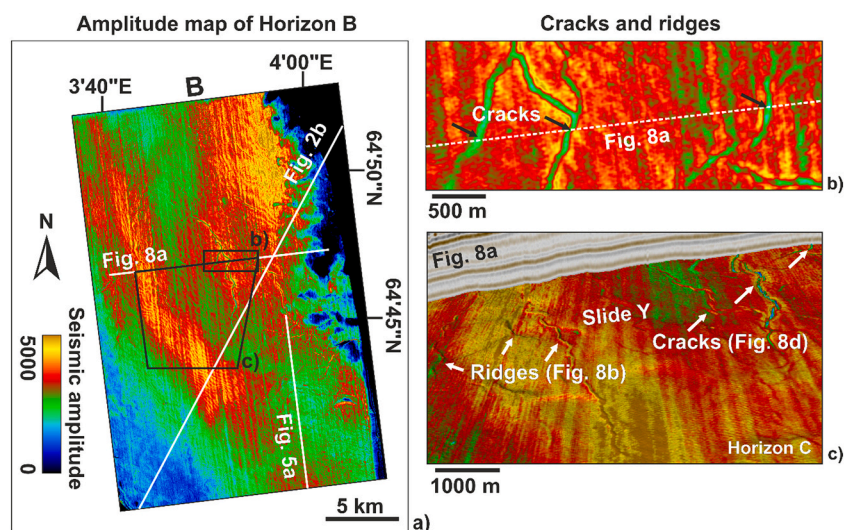


Fig. 9. a) Amplitude maps of Horizon B (2D view in a and b) and Horizon C (3D view in c) which are, respectively, positive and negative seismic reflections mapped below the top Naust W horizon. b) En-echelon and connected palaeo-seafloor cracks shown as local low-amplitude features. c) On the lower part of the slope, several ridges are observed as topographic highs at the level of Horizon C.

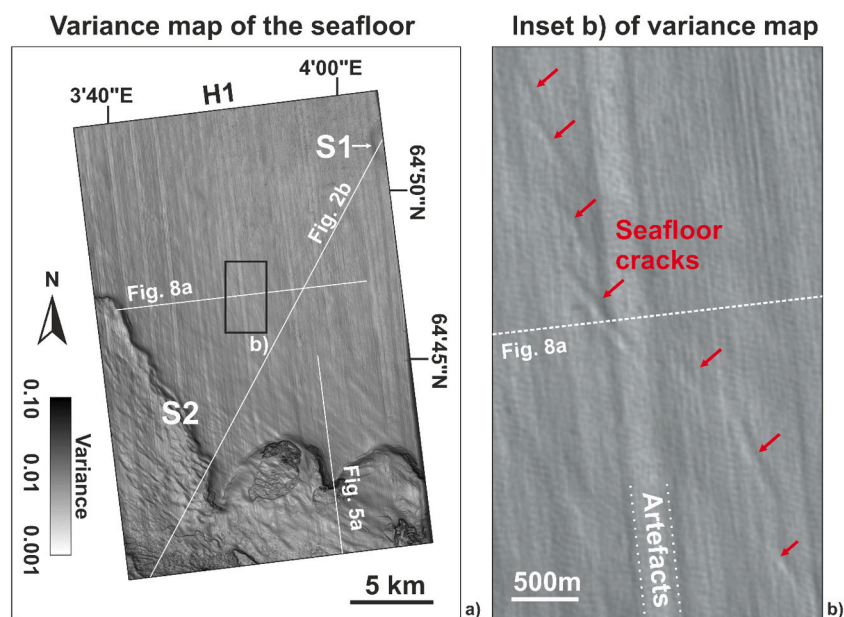


Fig. 10. a) Variance map of the modern seafloor (Horizon 1), and b) detail of seafloor cracks imaged on the same variance map. These en-echelon cracks are only observed on the variance maps using a logarithmic scale and are not clear on the interpreted seismic profiles (Fig. 8c).

2010; Reiche et al., 2011). Similar cracks to these in Fig. 11a, on Storegga's northeast flank, were interpreted as deriving from the dissolution of gas hydrates induced by rapid sedimentation and ocean warming during inter-glacial periods, and contributed to further fluid expulsion through pipes and pockmarks (Baeten et al., 2013; Hustoft et al., 2009; Karstens et al., 2018; Laberg et al., 2013; Mienert et al., 2010; Reiche et al., 2011). In this study, a group of seafloor cracks is observed above fluid flow features (palaeo-pipes) but showing no evidence for gas hydrate dissolution. This points, in the study area, to a different development of cracks from those recognised on the northeast flank of the Storegga Slide.

4.4. Buried ooze craters

Craters 1 to 3 (C1, C2 and C3) identified in this study have been partly described in the previous literature as 'craters B, C and D'

(Lawrence and Cartwright, 2010), 'craters near 6404/11-1' (Riis et al., 2005) or craters 2, 3 and 4 (Omosanya et al., 2022). Multiple processes have been proposed to explain the presence of ooze mounds downslope from the craters, including those favouring interactions between regional Slide W and local slides in the craters, and those stressing a close relationship between ascending oozes and crater-filling MTCs (Lawrence and Cartwright, 2010; Omosanya et al., 2022; Riis et al., 2005).

An important detail gathered in the study area is that ooze mounds are underlain by chaotic strata with slide blocks (Omosanya et al., 2022), i.e. they are markedly different from those craters located on the lower continental slope, where transparent seismic units are observed below ooze mounds (Lawrence and Cartwright, 2010; Riis et al., 2005). Similarly to Crater 1, located on the South Modgunn Arch (Song et al., 2020), Crater 2 consists of a central depression with a relatively high step formed in its downslope section (Fig. 12a and b). A group of E-W-

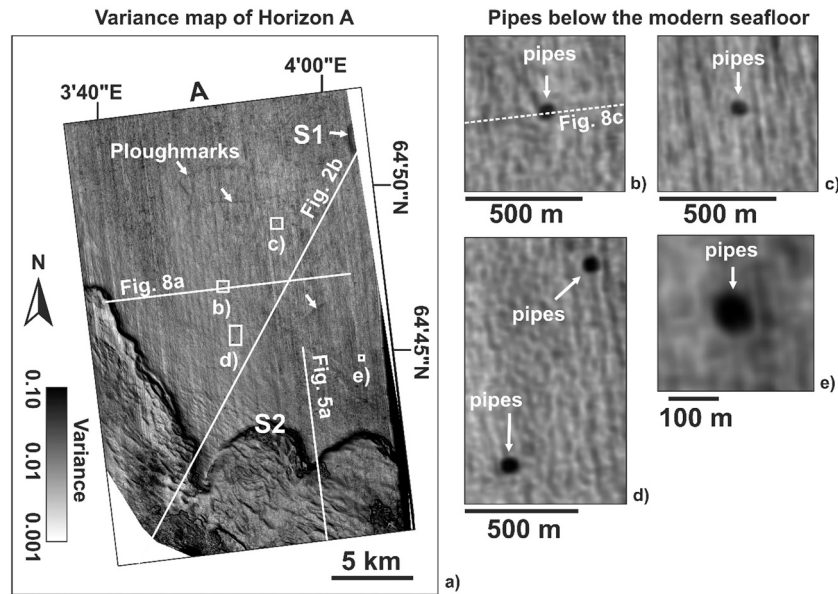


Fig. 11. a) Variance map of Horizon A, a positive reflector located ~40 ms twt below the modern seafloor. Ploughmarks are observed on the same horizon with a N85-N90 strike. b–e) Imaged fluid pipes are about 60 m wide.

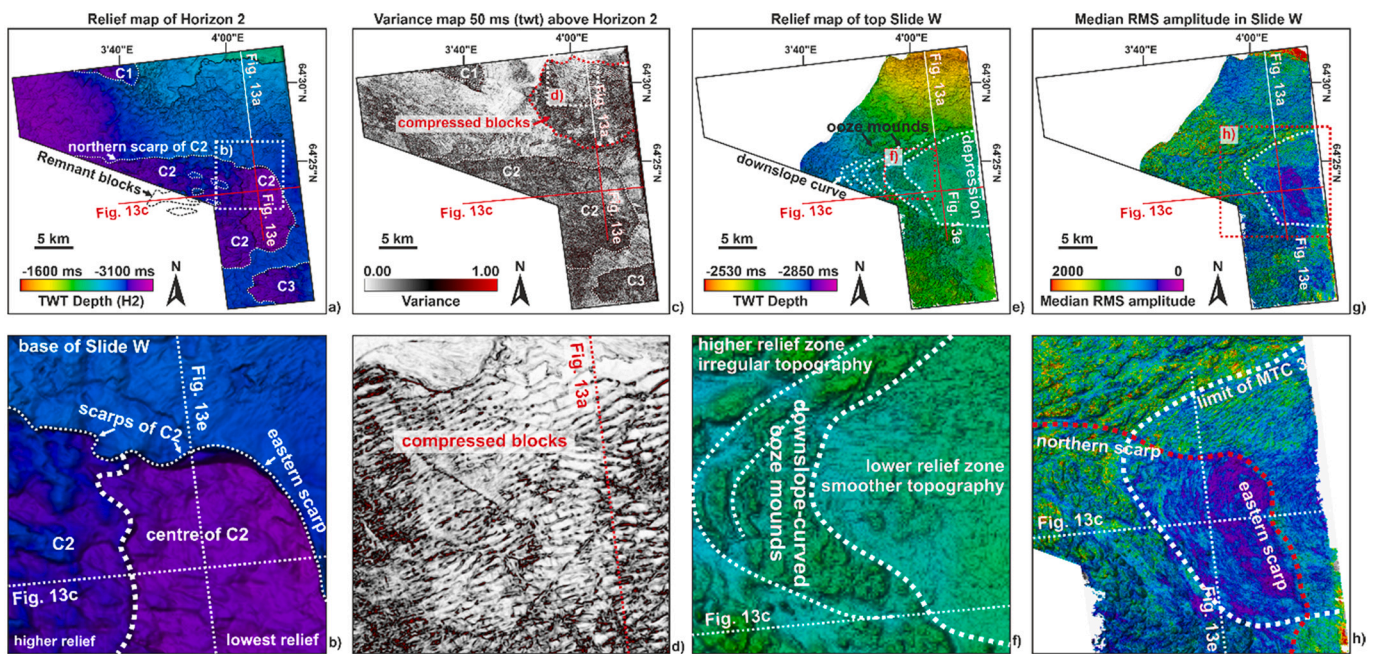


Fig. 12. a) and b) Two-way time structural map of basal glide plane (Horizon 2) showing craters (ooze evacuation structures) as local depressions in (a). A central crater is revealed in (b) within an area of low relief inside Crater 2, bounded by scarps (white dashed lines). C1, C2 and C3: Craters 1, 2 and 3; Remnant blocks are highlighted by dashed lines. c) and d) Variance map of a time slice 50 ms twt above the basal glide plane (Horizon 2) of slide blocks in (d). e) and f) Two-way time relief map of the top Slide W MTCs. A local depression is distinguished from the highly irregular topography on the lower slope. Downslope-curved features indicate the transport direction of ooze mounds and MTCs in the crater. g) and h) Median RMS amplitude map of Slide W, revealing ooze mounds, MTCs 2 and 3. The low-RMS amplitude zone on the upper part of the slope, highlighted by dashed lines, marks the location of MTC 3, correlating with the depression on the top of Slide W shown in (e). This low RMS amplitude zone covers Crater 2 from its eastern scarp.

trending blocks is also revealed beyond the northern scarp of Crater 2 by a variance map computed 50 ms twt above their basal glide plane (Fig. 12c and d).

Seismic profiles further image a group of thrust faults between discrete blocks (Fig. 13a and b). Although the top of this compression zone has been eroded by the Storegga Slide, as suggested by the overlying erosional surface (Fig. 13a), a gentle basal glide plane is still observed as a negative seismic reflection crossing the Kai Formation – in

effect forming a 1° glide plane between Horizons 3 and 4 (Fig. 13a and b). Close to its northern boundary, where thrust faults are better imaged, a scarp is identified as the last thrust fault separating compressed blocks from undeformed strata (Fig. 13b).

In the eastern part of Crater 2 (Fig. 12b), a depression herein called ‘central crater’ is bounded by a 100 ms twt (~ 70 m) tall scarp to the west, and 200 ms twt (~ 140 m) tall scarps to the north, east and south. These scarps separate the central crater from the relatively less faulted

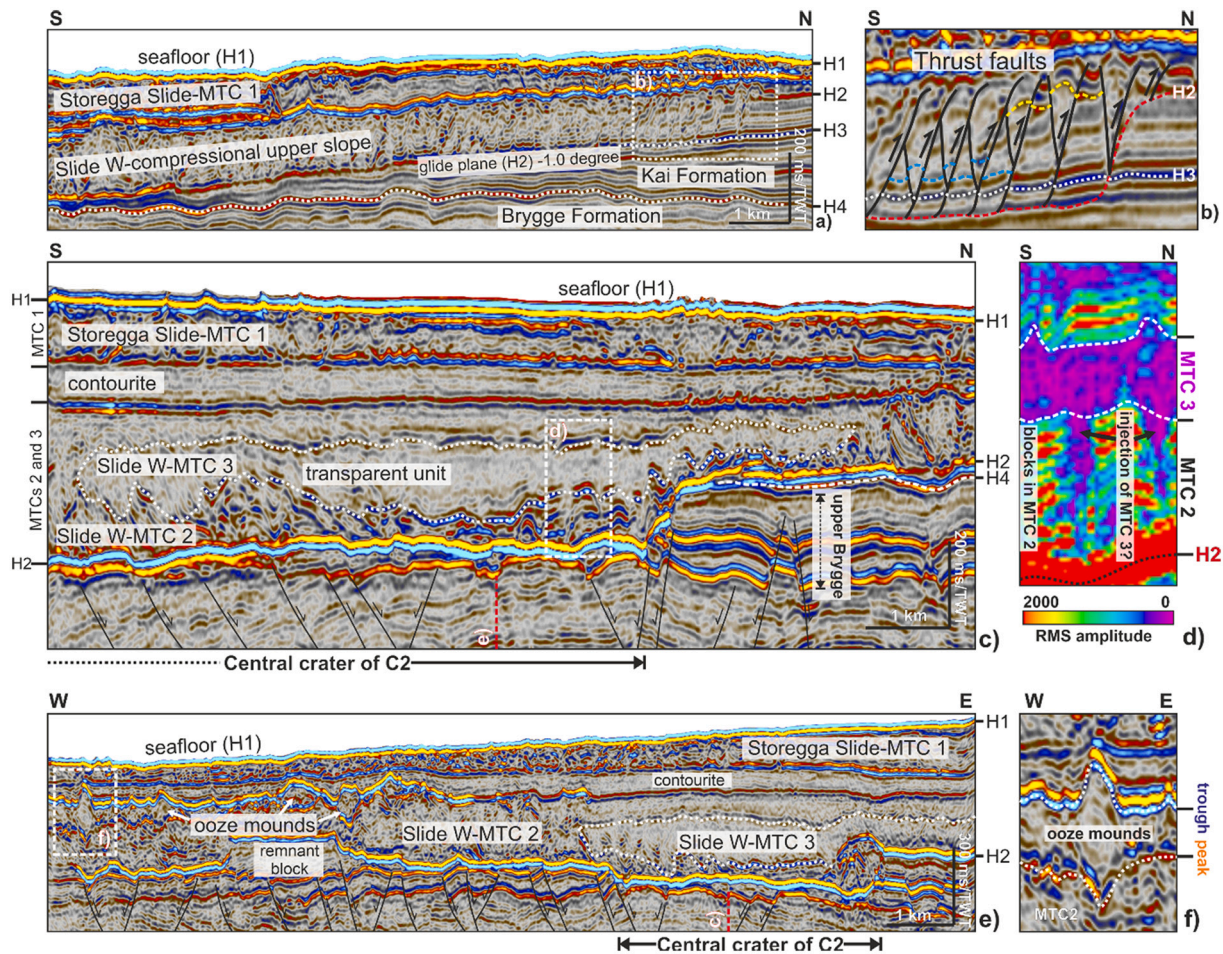


Fig. 13. Seismic profiles across Crater 2. Location of seismic profile shown in Fig. 12. a, b) Seismic profiles imaging the northern side of the central crater. Slide blocks and thrust faults are observed here. c, d) Two MTCs are identified in the central crater. MTC 2 shows chaotic seismic reflections and deformed blocks, resulting in a high RMS amplitude unit. MTC 3 covers MTC 2 as a transparent seismic reflection unit with low RMS amplitude. The top and base of MTC 3 are respectively positive and negative reflections. Part of MTC 3 is observed between underlying blocks in (d), suggesting a relationship between MTCs 2 and 3. e, f) A unit of ooze mounds is observed above MTC 2 on the lower side of the crater. These mounds can be distinguished by their symmetric positive and negative seismic reflections at their base and tops, respectively. MTC 3 covers the eastern scarp of Crater 2 towards the upper slope and bounds the ooze mounds on the lower slope.

upper Brygge Formation (Fig. 13c and e). A higher terrace in Crater 2 is observed beyond the west flank of the central crater and comprises remnant blocks (Figs. 12a and 13e). Below MTC 1, there are at least two Slide W-related MTCs inside Crater 2 based on the internal seismic character of strata filling it: a) MTC 2 fills the bulk of Crater 2 with chaotic reflections and higher RMS amplitude, while b) MTC 3 with lower RMS amplitude occurs as a transparent package covering MTC 2 from the east (Fig. 13c–e). MTC 3 can therefore be seen on RMS amplitude maps of Slide W to cover the eastern part of Crater 2, including its central depression and eastern scarp (Fig. 12g and h). The top and base of MTC 3 are respectively positive- and negative-amplitude reflections, making it an acoustically hard unit (Fig. 13c). Above MTC 3, a lower-relief zone on the top of Slide W reveals a smoother topography when compared with the strata around it (Figs. 12e and f and 13e).

5. Relationship amongst fluid pipes and recurrent landslides

Together with the recognition of regional Slides R and S, and local instability features such as ridges, en echelon cracks and Slide X, fluid pipes are identified in Terraces 1 and 2 in the form of localised vertical acoustic wipe-out zones on seismic profiles and associated high-variance and sub-circular features on attribute maps (Figs. 6, 7 and 11). At the level of Horizon E, the average diameter of these fluid pipes reaches 60 m, with local depressions or rises that are up to ~20 ms twt, i.e., ~14 m

(Fig. 7c). Some of these pipes are isolated, while others occur close to normal faults linked to polygonal faults in the Kai Formation, such as those imaged in Fig. 7b and c.

Pipes are still identified in Horizons A and D, but much less frequently and with no apparent variations in size (Figs. 6d and 11). The number of pipes in Horizon A approaches 15, decreasing to zero on the modern seafloor (Fig. 10). Together with other features in the Naust Formation, the spatial and temporal distribution of pipes and landslides across the upper continental slope (Terraces 1 and 2) is shown by the bar plots in Fig. 14.

Below the eastern part of Slide R, five (5) pipes are observed along its glide plane (see the pipes along Horizon 2 beneath Slide R in Fig. 14). Below Slide S, the number of fluid pipes decreases markedly from about 100 along Horizon B to only about 15 pipes right below its glide plane, focusing on its eastern part (see Horizon 2* beneath Slide S in Fig. 14). Most pipes terminate below this glide plane, rather than penetrating it.

A decreasing number of pipes is also observed across Slide X. At the level of Horizon E, the second reflection below Slide X, the abundance of pipes is about 130 with a focused distribution to the east (Figs. 7 and 14). Above Horizon E, the number of pipes decreases to about 70 at the base of Slide X (Fig. 14). Only approximately 30 pipes are observed along Horizon D (within Slide X) and also at the base of cracks and ridges identified along Horizon B (Figs. 6d and 14).

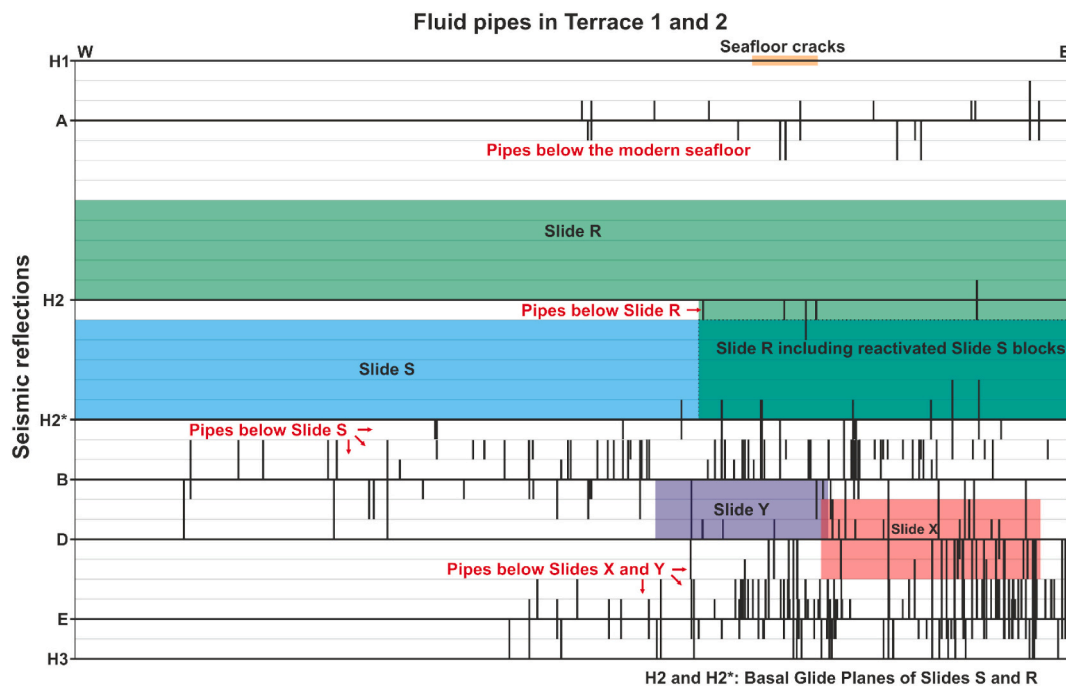


Fig. 14. Distribution of pipes in terraces 1 and 2. Vertical black lines represent the range of pipes, relative to key seismic reflections, including the seafloor (Horizon 1), a reflection below this latter (Horizon A), the basal glide plane beneath regional slides (Horizon 2 and 2*), seismic reflections recording early slides (Horizons B, D and E) and the top Kai reflector (Horizon 3). The abundance of pipes decreases below both regional slides (Slide R and S) and local slides (Slide X, Y and seafloor cracks).

6. Modelling of slide block generation and movement

To illustrate the evolution of slope instability in the study area after slope undercutting, four modelling scenarios are considered in this work. They represent the different settings identified in seismic data: 1) the effect of pre-existing MTCs on the continental slope, 2) the importance of glacial deposits as unstable intervals, 3) the formation of slope-propagating glide planes along a weak layer, and 4) the existence of multiple intervals with weak layers (Fig. 15). All scenarios were modelled considering a gently (1°), right-dipping slope with no-slip boundaries on their left side and below. The dip angle of the undercutting boundary on the lower slope was set at an angle of 30° relative to the continental slope (Fig. 15).

In the models completed in this paper, weak layers are considered as 8-m thick marine clays, obeying the vertical resolution of discrete seismic reflections in the Naust Formation (Roelofse et al., 2021) (Fig. 15c). In parallel, each failed interval is about 70-m thick, once again based on the average thickness of remobilised strata observed in seismic data (Figs. 4 and 5).

Based on published sediment core data, the initial strength of glacial deposits was, in the study area, set as 25 kPa at the seafloor, a value increasing with depth by 2.4 kPa/m (Gauer et al., 2005). Soft marine clays interbedded with glacial deposits were considered to have a homogeneous strength of 5 kPa (L'Heureux et al., 2012). The sensitivity of glacial deposits and marine clay was set at 3 and 7, respectively (L'Heureux et al., 2012, 2013). The description, and absolute values of other physical parameters are included in Supplementary File 1.

6.1. Scenario 1 – Sediment creep through the reactivation of older, pre-existing MTCs

Together with geochronological data, which proves that slope undercutting along a 'L'-shaped pathway occurred after the main Storegga Slide event (Hafliðason et al., 2005), chaotic seismic reflections indicate that MTCs were deposited in the study area before slope undercutting occurred along Scarp 5. Revealing a constant low shear strength, the

residual strength of marine clay, sediment creep is observed in Scenario 1 at $t = 10$ s and could be expected to continue in time (Fig. 15a). Except for its frontal elongation, no particular structures are observed within this fully softened and deformed interval (Fig. 15a).

6.2. Scenario 2 – Frontal collapse of glacial deposits

To illustrate the sensitivity of the continental slope to the physical properties of its strata, and thus highlight the effect of weak layers in controlling slope stability processes, Scenario 2 considered an interval comprising glacial deposits with the same initial geometry of Scenarios 1 and 3 (Fig. 15b). Compared to the relatively soft MTCs modelled in Scenario 1, the relatively harder glacial deposits show increasing strength with depth and limited slope failure in the toe area at $t = 9000$ s, a much longer period than that considered in Scenario 1 (Fig. 15a and b). In addition, the frontally collapsed part of the MTC was separated from relatively intact slope strata by a softened zone recording the lowest strength ratio (see light blue area in Fig. 15b). Similar failure styles are identified in the toe regions of MTCs and associated with the presence of homogeneous sediment (Steward et al., 2011; Taylor, 1937).

6.3. Scenario 3 – Upslope propagation of instability after slope is undercut

Both the seismic data in this study and the published research (Kvalstad et al., 2005; L'Heureux et al., 2012, 2013) suggest the presence of soft marine clay in between harder glacial deposits. Hence, Scenario 3 considered the deformation of a 62-m thick glacial interval over a 8-m thick marine clay (Fig. 15c).

At $t = 10$ s, a glide plane propagates along a weak layer (marine clay) towards the upper slope (Fig. 15d). At this stage (1), even though the strength of the weak layer is reduced to its residual strength after the continental slope is undercut, no further deformation is observed in the harder glacial deposits above (Fig. 15d). However, together with the softening of the basal weak layer, slope instability is shown to propagate to the upper slope. At $t = 200$ s, a group of faults develops on the upper slope via the concentration of softening in parts of the glacial deposits

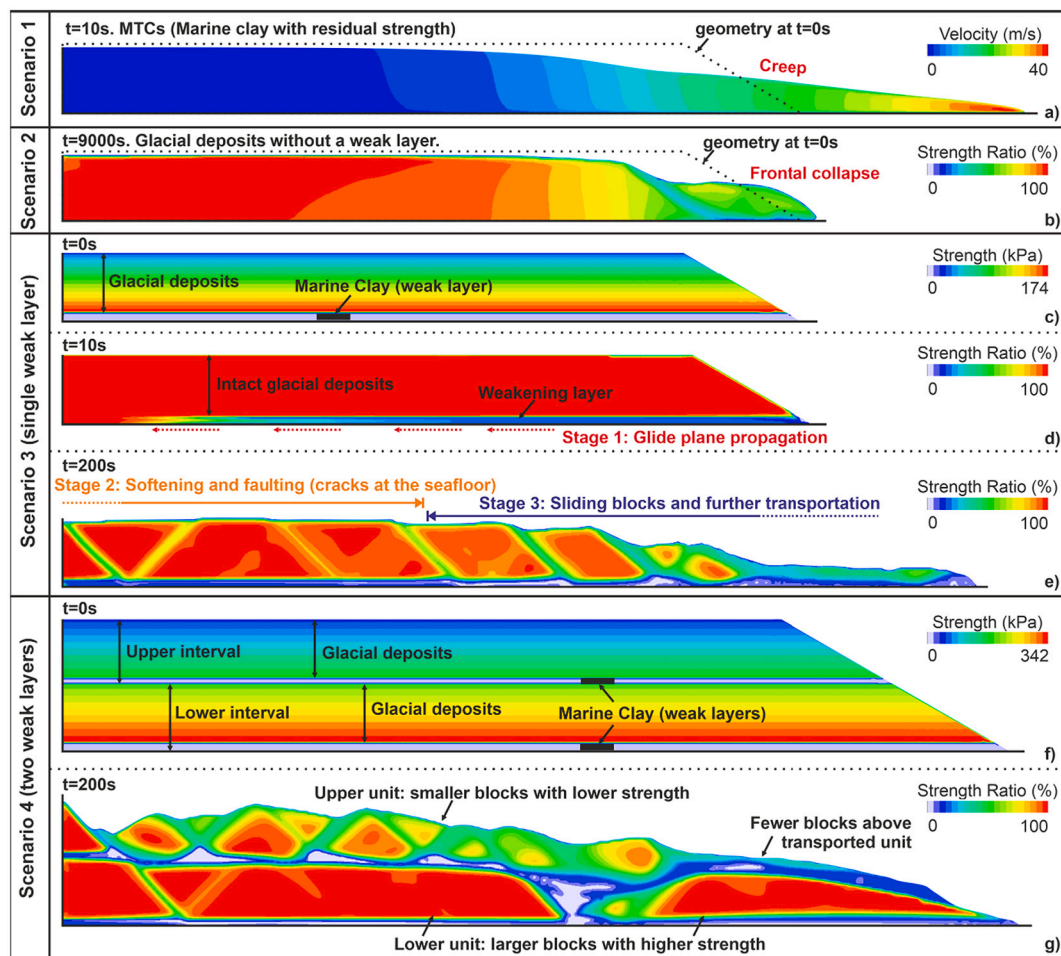


Fig. 15. Computational fluid dynamics (CFD) models completed in this work. All models are set on a gentle (1°), right-dipping slope with no-slip boundaries at the bottom and left. **a)** Scenario 1: The undercut slope is composed of MTCs with a homogeneous, but weak, constant residual strength that resembles that of marine clay. The dashed line represents the initial geometry of the slope. The elongation of the slope strata after movement is initiated suggests sediment creep predominates when pre-existing MTCs are undercut. **b)** Scenario 2: The slope is composed of glacial deposits without a weak bottom layer. The initial geometry is similar to Scenario 1. Frontal collapse is observed in a much longer period ($t = 9000$ s) and restricted to the frontal part of the undercut slope. **c–e)** Scenario 3: Following the initial geometry of Scenarios 1 and 2, slope strata consist of 62-m thick glacial deposits with a 8-m thick marine clay at the bottom. In **d)**, $t = 10$ s, the scenario reflects glide plane propagation (stage 1) due to a fast weakening of the basal layer. Later in **e)**, at $t = 200$ s, slope failure develops in two distinct stages, stages 2 and 3, which reflect the development of softening and faulting in slope strata with no apparent sliding (stage 2), to fully detached coherent units and translated slope strata (stage 3). **f, g)** Scenario 4: Two intervals similar to Scenario 3 (**c)** are vertically stacked in (**f)** considering an increase in the initial strength of glacial deposits with depth. Two distinct units of slide blocks are developed with differing strength and geometry due to the presence of an intermediate weak layer separating the stacked intervals.

overlying them, thus forming cracks on the sea floor and fractures below (Stage 2 in Fig. 15e). Further softening of strata in the lower slope occurs in a third stage, when the unit above the marine clays is fully detached and develops a series of slide blocks (Stage 3 in Fig. 15e).

6.4. Scenario 4 – Vertically stacked intervals with weak layers

Scenario 4 considers the two intervals modelled in Scenario 3 to be vertically stacked (Fig. 15f). The initial strength of glacial deposits once more increases with depth by 2.4 kPa/m. After $t = 200$ s, two units with slide blocks are observed due to a decrease in strength along softened zones (in this case, faults) formed between coherent triangular and trapezoidal blocks (Fig. 15g). Compared to the lower unit, the upper one has a lower strength at the start of the model ($t = 0$ s in Fig. 15f) and is deformed into a series of smaller blocks (Fig. 15g). Upslope, the upper unit with slide blocks is relatively well preserved and overlies a lower unit still with no apparent downslope movement (Fig. 15g). On the lower slope, a fully detached lower unit with slide blocks corresponds to a third stage of instability – further strain-softening occurs both inside

and above the lower unit, while the upper unit loses its strength and internal coherence (Fig. 15g).

Based on the developed models, Scenario 4 is the one that most approaches the setting of the study area. This does not mean that Scenarios 1 to 3 do not apply to parts of the northwest flank of the Storegga Slide – in fact, they may be locally more important than Scenario 4. However, the recurrence of submarine landslides imaged in seismic data is better explained by the triggering of new MTCs above older, weaker MTCs.

7. Discussion

7.1. What features are diagnostic features of an unstable seafloor?

In the study area, scarps S1, S2 and S3 were initially formed during Slides S and R, and delimit intervals with specific MTCs and glide planes. In contrast to the seafloor cracks observed on the upper continental slope (Nyegga area), where local extension occurred due to sediment evacuating the lower slope during the Storegga Slide (Reiche et al., 2011), both scarps S1 and S2 (limiting Terrace 1) were originally formed

before the Storegga Slide. In addition, the variance map in Fig. 10b shows a group of seafloor cracks in Terrace 1 over an interval denoting fluid expulsion (Figs. 8c, 11b and 16). This shows that reduced lateral support does not solely explain the generation of these extensional cracks.

A group of echelon cracks is observed along the outer shelf edge to the north of the main Storegga Slide headwall, and is here suggested to have been preconditioned by fluid expulsion following gas-hydrate dissociation (Mienert et al., 2010). Considering there is also an interval of significant fluid expulsion (pipes) beneath the cracks mapped in this work (Figs. 10 and 11) without a directly underlying BSR, we propose the build-up of shallow pore overpressure as being responsible for these same extensional cracks, a similar process to that recorded along the Atlantic margin of the United States of America (Hill et al., 2004). Even though there are no pockmarks on the seafloor of the study area, fluid pipes were able to increase pore pressure in shallow sediment and thus reduce the strength of an incipient glide plane formed below the observed seafloor cracks. Compared with the 0.5° glide plane below Slide Y, the gradient of the modern seafloor approaches 1.3° , a similar value to the glide plane of Slide X (Figs. 5a and 8a). Such a slope gradient can further promote slope instability by inducing local changes in shear stress. Hence, if pore overpressure or slope gradient continue to increase, the modern seafloor can be the locus of future slope failure.

Above Slide X, which is interpreted as a blocky MTC near Horizon D (Fig. 6a and 16), another style of slope instability is recorded in Horizon B, where extensional cracks and compressional ridges show similar strikes (Figs. 9c and 16). This new MTC is named Slide Y in this work. The co-existence of cracks and ridges between the top of Naust W and Horizon D suggests they deformed the palaeo-seafloor at the same time. One explanation for their formation is that the parallel cracks and ridges were driven by different processes, but their development was limited to a specific interval. While we found no evidence to support this hypothesis, there is no other slide feature beyond these narrow cracks and ridges. It is therefore clear that slope instability was limited to the interval between the top of Naust W and Horizon D, and strata above and below were not affected by this same instability event. Considering that the cracks are in the shallowest part of the study area, while compressional ridges occur lower on the continental slope (Figs. 9c and 16), Slide Y was apparently formed by the effect of gravity. Thus, even though a glide plane following a seismic reflection is hard to identify in Slide Y, in seismic data, we propose that this style of slope instability, comprising

cracks and ridges in Horizons B and C, results from local slope failure above Horizon D (cracks and ridges in Figs. 9 and 16).

7.2. Evolution models explaining the formation of Crater 2

In this study, three craters (Craters 1 to 3) are interpreted in seismic data and Crater 2 has been thoroughly mapped (Figs. 12 and 13). Beyond its northern scarp, the overlapping of shortened thrust blocks with E-W strikes indicates extrusion of sediment from the south and confinement to the north (Lawrence and Cartwright, 2009) (Figs. 12c and d, 13b and 17). Considering that our study area is located on the lower slope of Slide W, this confinement should result from the fact that Slide W is bounded by the northwest flank of the Storegga area. Importantly, both the longitudinal remnant blocks in Crater 2 (Figs. 12a and 17) and the local downslope-curved ooze mounds (Figs. 12f and h and 17) reveal an westward mobilisation of MTCs inside Crater 2, similarly to other craters nearby (see craters 2–4 in Omosanya et al., 2022). This difference in transport directions between the MTCs above Slide W and crater-filling strata suggests that the emplacement of MTCs followed two models: a) a regional northwest transport of MTCs from the upper continental slope, and b) local westward transport of crater-filling MTCs in a downslope direction.

The development of these two models can be described as follows; in the first model, a local slide would have been triggered by ooze evacuation and was then mobilised together with a regional slide (Lawrence and Cartwright, 2010). In the second model, ooze evacuation was induced by overlying MTCs, which then transported the oozes within a local slide (Lawrence and Cartwright, 2010; Riis et al., 2005). The first model implies the generation of simultaneous slides inside and outside Crater 2, not agreeing with our interpretation of two directions of transport in Slide W. Our results support the second model, and we evoke distinct steps in the formation of the ooze mounds in the study area: Step 1) a regional Slide W was first transported in a northwest direction and limited by the northern flank of the Storegga Slide (the northern scarp of Crater 2 in Figs. 12b and 18b); and Step 2) a local slide inside Crater 2 followed step 1 and transported the evacuated oozes downslope (Figs. 12f, 17 and 18c).

Within the crater-filling MTCs, our seismic data show a transparent seismic unit, MTC 3, which is distinct from the chaotic, high-amplitude reflections that are typical of MTC 2 (Figs. 12h and 13d). MTC 3 drapes the eastern scarp of Crater 2 on the upper continental slope and bounds

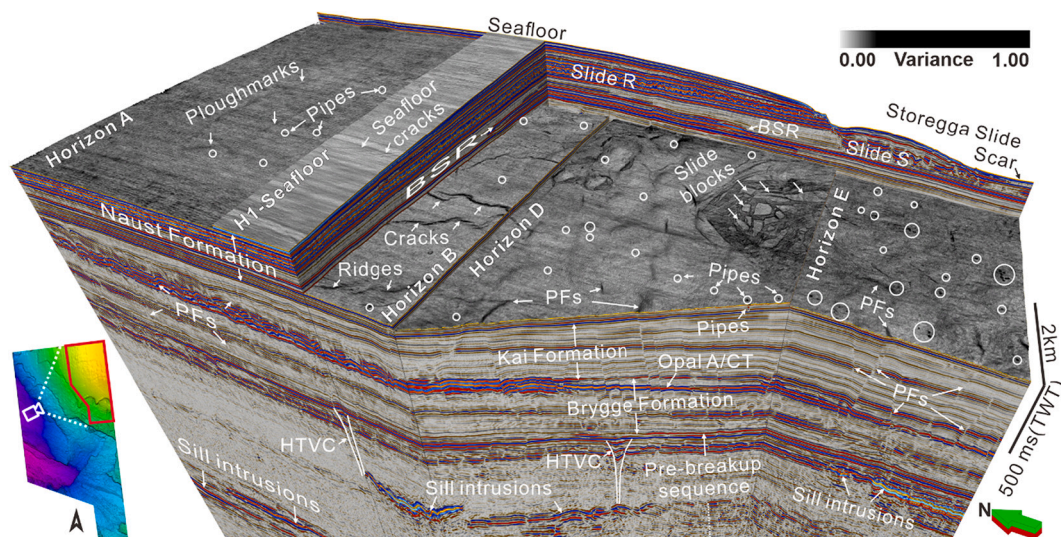


Fig. 16. 3D view of features related to slope instability in Terrace 1 and 2, including seafloor cracks (detail in Fig. 10b), ploughmarks (detail in Fig. 11a), pipes marked as circles (detail in Fig. 14), cracks and ridges representing a palaeo-slope failure (Slide Y in Fig. 9), local slide blocks (Slide X in Fig. 6). Other related fluid-flow features are highlighted such as polygonal faults, BSRs, HTVCs (hydrothermal vent complexes), PFs (polygonal faults), an Opal A/CT transition zone, and sill intrusions.

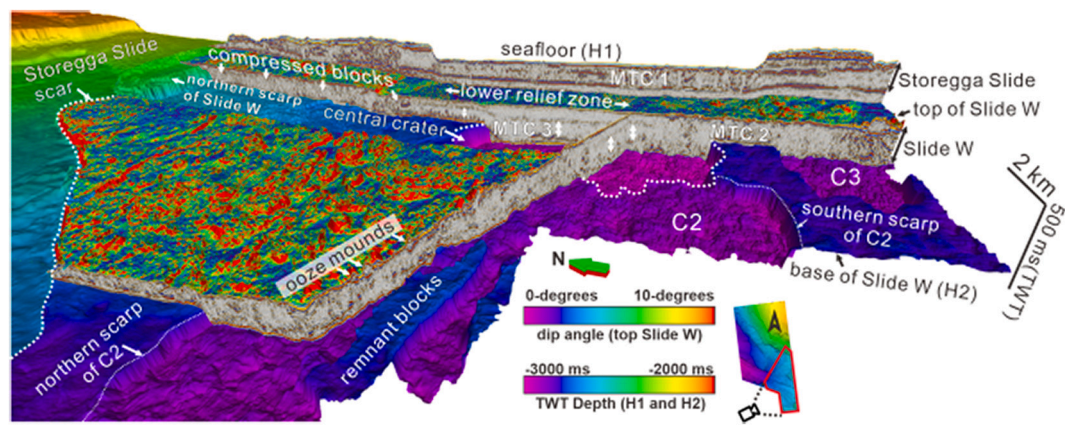


Fig. 17. A 3D view of Crater 2 and related features, including compressed blocks on the upper part of the slope (detail shown in Fig. 12d), MTCs 2 and 3 (see Figs. 12h, 13c, d and e), remnant blocks on the lower part of the slope and overlying ooze mounds (detail in Figs. 12f and 13e and f). The top of Slide W is shown on a dip map, highlighting the difference between the gentle depression above MTC 3 and the ooze mounds on the lower part of the slope.

the ooze mounds on the lower slope (Figs. 12f and h, 13e and 17), whereas MTC 2 is observed below both the ooze mounds and MTC 3 but disappears outside the eastern scarp in Fig. 13e. The direct contact observed between MTC 3 and the ooze mounds (Figs. 12h and 13e) suggest these low-density oozes ascended to the palaeo-seafloor (as ooze mounds) no earlier than MTC 3 filled the crater, otherwise MTC 3 would have intruded the ooze mounds from below. Considering that the ooze evacuation structure (crater) C2 is filled by MTCs, the ascending process of oozes and the downslope transport of crater-filling MTCs would have occurred at the same time (Fig. 18c).

In the central crater, several high-amplitude blocks are observed between MTC 3 and its underlying oozes (Fig. 13c and e). The gaps between these slide blocks are filled by MTC 3 (Fig. 13d), suggesting a close relationship amongst oozes, MTC 2 and MTC 3. Together with the contact between MTC 3 (upper slope) and the ooze mounds on the lower slope (Fig. 12h), we suggest MTC 2 to comprise a mixture of mobilised oozes with failed Naust W strata; after Slide W was deposited over the low-density oozes (MTCs above the Brygge Formation in Fig. 18b), the latter were remobilised and ascended to the palaeo-seafloor as mounds (ooze mounds in Figs. 13f and 18c). At this time, the liquefied oozes mixed with the overlying MTCs, the chaotic seismic interval that is now MTC 2 (Figs. 13d and 18c). Together with the downslope transport of ooze mounds and MTC 2, MTC 3 flowed into Crater 2 from the upper continental slope as a transparent seismic unit crossing its eastern scarp (MTC 3 in Figs. 13e and 18c). The base of Crater 2 was thus filled by MTC 3, resulting in a central crater with deformed oozes blocks (deformed blocks in Figs. 13c and 18c). Apart from the loading imposed by Slide W, other triggers of ooze liquefaction in the study area may include pore overpressures by fluid migration through polygonal fault systems and hydrothermal vent complexes (Lawrence and Cartwright, 2010; Omsonya et al., 2022; Roelofse et al., 2021; Song et al., 2020).

7.3. Cyclic overpressure as a likely trigger of slope instability prior to Slide W (~1.7 Ma)

The deformation styles observed around the Storegga Slide, including Slides X and Y, reveal that gravitational processes were key drivers of slope failure. However, considering the gentle slope of the study area, recording an average value of just 0.5°, other factors may have contributed to slope instability such as fluid flow below the glide planes of Slides R, S, Y and X (Figs. 14 and 16).

Fluid pipes have been widely observed on the mid-Norwegian margin near the Nyegga, Troll, Morvin and Haltenpipe fields (Hovland et al., 2010; Hustoft et al., 2009; Karstens et al., 2018). In the study area, we found several intervals with fluid pipes in the glacially controlled Naust Formation (Figs. 14 and 16). Inside the Naust W interval, the

oldest interval in the Naust Formation above polygonally faulted oozes, fluid flow is revealed in the form of abundant fluid pipes, including both isolated pipes and pipes associated with faults (Fig. 7). Fluid pipes are mainly observed 40 ms twt (~28 m) above the Kai Formation, suggesting significant fluid expulsion after Naust W was deposited (Fig. 14).

One possible source of excess pore pressure in the study area, strong enough to generate hydraulic fractures and associated fluid pipes, is fluid accumulated beneath more impermeable layers (Cartwright and Santamarina, 2015). Changes in the gas hydrate stability zone (GHSZ) can lead to gas-hydrate dissociation and subsequent fluid migration towards the seafloor (Crémière et al., 2016). Along the northern flank of the Storegga Slide, a modern BSR marking the base of the GHSZ is observed ~300 m below the seafloor, and is limited to the Naust Formation (Bünz et al., 2003). Since the last glacial maximum, glaciation-induced changes in bottom-water temperature and eustatic sea level resulted in a ~10 m to ~100 m rise of the BSR between the continental shelf (at a water depth of about 500 m) and the lower continental slope, at a depth of about 900 m (Mienert et al., 2005). However, the water depth in the study area exceeds 1000 m, which is beyond the water depth in which glaciations influenced the GHSZ. This condition indicates the dissolution of gas hydrates was unlikely during the deposition of Naust W, as well as correlating fluid flow and pore overpressure.

Considering that pipes are also observed around the top of the ooze-rich pre-Quaternary Brygge and Kai Formations (Song et al., 2020), the dehydration of oozes and corresponding fluid migration should have occurred before the Quaternary, together with temperature-controlled diagenetic transformations from high-porosity and low-density opal-A to low-porosity and high-density opal-CT (Awadalkarim et al., 2014; Chand et al., 2011). As the Opal A/CT transition zone imaged in the study area does not follow the modern seafloor and was locally uplifted (Figs. 2b and 16), this diagenetic front was likely formed during Miocene-Pliocene tectonic compression and later became inactive, leaving behind a fossilized Opal A/CT transition zone (Davies and Cartwright, 2002; Neagu et al., 2010). Thus, even though biogenic methane from oozes could still migrate through polygonal faults and pipes (Chand et al., 2011), fluid originating from this Opal A/CT transition zone is not the reason for the short-term fluid expulsion documented in this study.

In the interval above Slide R, up to the modern seafloor, the coexistence of pipes and east-west ploughmarks is clear along Horizon A (Figs. 11 and 16). Considering their distribution on the outer mid-Norwegian margin (Fig. 1a) where northeast-flowing currents dominate since Quaternary, these east-west ploughmarks correlate with a catastrophic iceberg discharge and transport event, which left ploughmarks with strikes near, or slightly beyond, N90 degrees (Montelli et al., 2018). Therefore, based on the coexistence of ploughmarks and pipes,

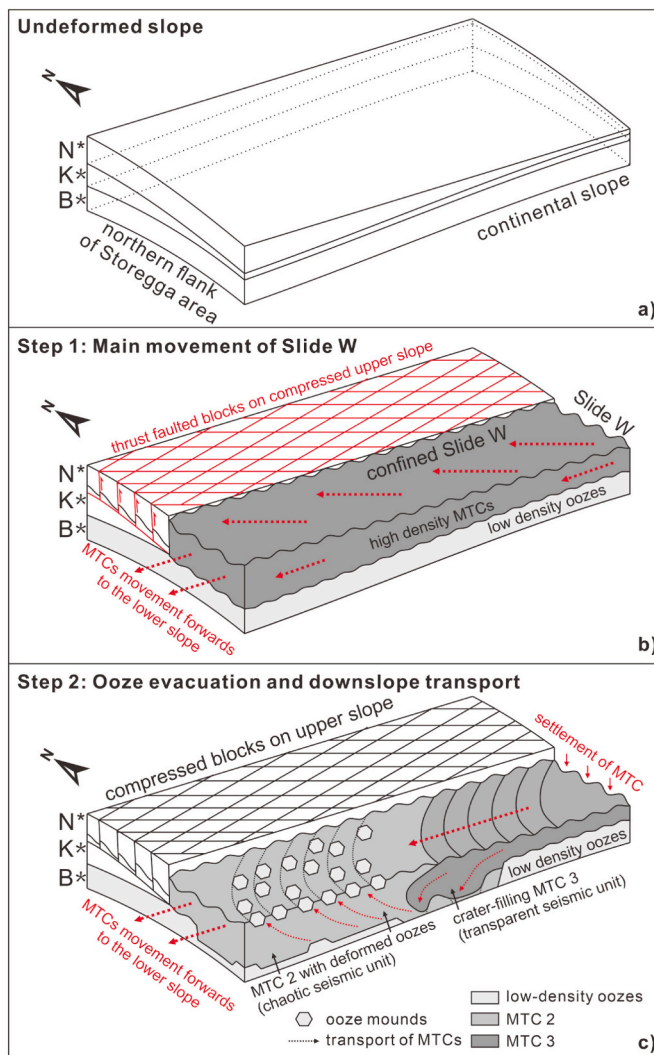


Fig. 18. Schematic diagram summarising the development of Crater 2. **a)** Inferred undeformed slope at the northwest flank of the Storegga Slide, mid-Norwegian margin. **b)** Step 1: main Slide W event on the continental slope. As the northwest transport of Naust W was confined by the northwest flank of the Storegga Slide, an interval of compressed blocks was generated with thrust faults inside. The base of these blocks crosses the entire Kai Formation. On the eroded lower slope. The low-density oozes were directly loaded by Slide W. **c)** Step 2: after being loaded by high-density MTCs, the low-density oozes in Brygge Formation were deformed, mobilised and partly liquefied, leading to the ascending process of oozes to palaeo-seafloor as mounds, and the mixture of overlying MTCs with oozes to form MTC 2. In parallel, the downslope transport of MTC 2 and ooze mounds is accompanied by the transport of MTC 3 from the upper continental slope. N*: Naust W Formation. K*: Kai Formation. B*: Brygge Formation. SMA: South Modgunn Arch.

the formation of these shallow fluid-flow features (pipes) in the Naust Formation is, in this work, associated with recurrent deglaciation periods.

Rapid deposition and sediment compaction during interglacial periods is known to enhance lithological and permeability anisotropies and, thus, the sub-surface accumulation of fluid (Bryn et al., 2005; Leynaud et al., 2007; Trincardi et al., 2004). During the last (Weichselian) interglacial stage, extremely high sediment loads on the mid-Norwegian margin increased pore fluid pressure in the Nyegga area, leading to extensive fluid venting before the onset of the Storegga Slide (Hustoft et al., 2009). Therefore, the coexistence of ploughmarks and pipes, cyclic fluid flow below Slides X, Y, S, R, and seafloor cracks (Figs. 14 and 16), is interpreted here to result from the rapid compaction

of sediment in glacial-marine strata, with a resulting build-up of excess pore pressure long enough to generate hydraulic fractures (Elger et al., 2018). Similarly to other Quaternary slides around the headwall of the Storegga Slide, the decreased effective vertical stress resulting from excess pore pressure in specific intervals further enhanced slope instability by reducing the shear strength of sediment (Bellwald et al., 2019; Leynaud et al., 2009; Leynaud et al., 2004). These hydraulic fractures were also able to release overpressure from permeable layers, at the same time preventing the further triggering of landslides (Kaminski et al., 2020).

Compared to parts of Horizon E, where the average slope gradient is $\sim 0.5^\circ$ (Fig. 8a), the glide plane beneath Slide X reaches a value close to 1.0° , the steepest in the study area (Fig. 5a). For a submarine landslide to occur above a gentle glide plane $< 1.0^\circ$, reduced support at the toe is thought to be the key precondition for its onset, promoting an increase in shear stress along the glide plane (Micallef et al., 2007). Additionally, local onlap geometries in seismic data suggest there was no effective lateral support to the toe of Slide X before it was mobilised (Fig. 5a). Thus, Slide X was likely triggered by the combined build-up of excess pore pressure, local slope oversteepening, and the loss of lateral (and toe) support in deeper parts of the continental slope, conditions that were similar to those recorded by the younger Slides S and R (Bull et al., 2009).

8. Conclusions

The Storegga Slide complex on the mid-Norwegian margin has recorded multiple, recurrent slope failures for the last 2.6 Ma, concomitantly with the deposition of the glacial-marine Naust Formation. In this study, the interpretation of high-resolution seismic from the northwest flank of the Storegga Slide area recognised two (2) local slope failures, preceding the first regional-scale landslides, as features marking the onset of Quaternary slope instability on the mid-Norwegian margin. The recognition of Mass-Transport Complexes (MTCs) with distinct seismic characters above a crater confirm the development of ooze evacuation structures during a first regional landsliding event. Importantly, seafloor cracks indicate the areas where further instability may occur in the future. The main conclusions of this paper are as follows:

a) Blocks in Slide X, and local features in Slide Y, comprise evidence for early slope instability on the mid-Norwegian margin. Fluid accumulation within glacial-marine deposits was a primary factor promoting this early instability phenomenon.

b) Different transport directions of MTCs inside and outside Crater 2 suggest that ooze evacuation occurred after slope strata were loaded by high-density MTCs during Slide W. An acoustically hard unit covering the eastern scarp of Crater 2 further indicates the ascending movement of oozes, with this ascension being accompanied by the downslope mobilization of ooze mounds and crater-filling MTCs.

c) A group of seafloor cracks above regional pipes suggest an early stage of slope failure on the present-day seafloor. Similarly to Slides X and Y, these seafloor cracks were likely preconditioned by fluid accumulated below them and losses in lateral support (slope undercutting).

d) Compared to regional slope failure events such as the Storegga Slide, Slides W, S and R, local slope failure is rare in the study area at present. However, early phases of instability and related slope deformation may reveal the factors responsible for the initiation of long-term slope instability, and the areas predisposed for future slope failure. Based on the detailed interpretation of older landslides, further slope instability is still possible near the northern flank of the Storegga Slide.

Declaration of Competing Interest

The authors declare that they have no known competing financial interests or personal relationships that could have appeared to influence the work reported in this paper.

Data availability

The seismic data (Survey MC3DMGS2002) that support the findings are available from the Norwegian University of Science and Technology (NTNU). Restrictions apply to the availability of these data, which were used under license for this study. Data are available with permission of NTNU.

This research did not receive any specific grant from funding agencies in the public, commercial, or not-for-profit sectors.

Acknowledgements

We acknowledge the permission conceded by Norwegian University of Science and Technology (NTNU) – Norwegian Petroleum Directorate – Schlumberger Petrel Ready Database for the use of the seismic and borehole data presented in this paper. Schlumberger (providers of Petrel®) is acknowledged for the provision of the academic licenses to Cardiff University's 3D Seismic Laboratory. We thank Editor-in-chief Michele Rebesco, Greg Moore (Hawaii) and three anonymous reviewers for their constructive comments.

Appendix A. Supplementary data

Supplementary data to this article can be found online at <https://doi.org/10.1016/j.margeo.2022.106933>.

References

- Alves, T.M., 2012. Scale-relationships and geometry of normal faults reactivated during gravitational gliding of Albian rafts (Espírito Santo Basin, SE Brazil). *Earth Planet. Sci. Lett.* 331, 80–96. <https://doi.org/10.1016/j.epsl.2012.03.014>.
- Awadalkarim, A., Sørensen, M.K., Fabricius, I.L., 2014. Petrophysical analysis of siliceous-ooze sediments, More Basin, Norwegian Sea. *Petrophysics* 55, 333–348.
- Baeten, N.J., Laberg, J.S., Forwick, M., Vorren, T.O., Vanneste, M., Forsberg, C.F., Kvalstad, T.J., Ivanov, M., 2013. Morphology and origin of smaller-scale mass movements on the continental slope off northern Norway. *Geomorphology* 187, 122–134. <https://doi.org/10.1016/j.geomorph.2013.01.008>.
- Bellwald, B., Urlaub, M., Hjelstuen, B.O., Sejrup, H.P., Sørensen, M.B., Forsberg, C.F., Vanneste, M., 2019. NE Atlantic continental slope stability from a numerical modeling perspective. *Quat. Sci. Rev.* 203, 248–265. <https://doi.org/10.1016/j.quascirev.2018.11.019>.
- Berg, K., Solheim, A., Bryn, P., 2005. The Pleistocene to recent geological development of the Ormen Lange area. *Mar. Pet. Geol.* 22, 45–56. <https://doi.org/10.1016/j.marpetgeo.2004.10.009>.
- Berndt, C., Skogly, O.P., Planke, S., Eldholm, O., Mjelde, R., 2000. High-velocity breakup-related sills in the Vøring Basin, off Norway. *J. Geophys. Res. Solid Earth* 105, 28443–28454. <https://doi.org/10.1029/2000JB900217>.
- Berndt, C., Büinz, S., Clayton, T., Mienert, J., Saunders, M., 2004. Seismic character of bottom simulating reflectors: examples from the mid-Norwegian margin. *Mar. Pet. Geol.* 21, 723–733. <https://doi.org/10.1016/j.marpetgeo.2004.02.003>.
- Berstad, I.M., Sejrup, H.P., Klitgaard-Kristensen, D., Hafliadason, H., 2003. Variability in temperature and geometry of the Norwegian Current over the past 600 yr; stable isotope and grain size evidence from the Norwegian margin. *J. Quat. Sci.* 18, 591–602. <https://doi.org/10.1002/jqs.790>.
- Bondevik, S., 2019. Tsunami from the Storegga Landslide, Encyclopedia of Complexity and Systems Science. https://doi.org/10.1007/978-3-642-27737-5_644-1.
- Bondevik, S., Stormo, S.K., Skjerdal, G., 2012. Green mosses date the Storegga tsunami to the chilliest decades of the 8.2 ka cold event. *Quat. Sci. Rev.* 45, 1–6. <https://doi.org/10.1016/j.quascirev.2012.04.020>.
- Brekke, H., 2000. The tectonic evolution of the Norwegian Sea continental margin, with emphasis on the Vøring and More basins. *Geol. Soc. Lond.* 167, 327–378.
- Brown, A.R., 2011. Interpretation of Three-Dimensional Seismic Data. Society of Exploration Geophysicists and American Association of Petroleum Geologists.
- Bryn, P., Solheim, A., Berg, K., Lien, R., Forsberg, C.F., Hafliadason, H., Ottesen, D., Rise, L., 2003. The Storegga Slide Complex; Repeated Large Scale Sliding in Response to Climatic Cyclicity, pp. 215–222. https://doi.org/10.1007/978-94-010-0093-2_24.
- Bryn, P., Berg, K., Forsberg, C.F., Solheim, A., Kvalstad, T.J., 2005. Explaining the Storegga Slide. *Mar. Pet. Geol.* 22, 11–19. <https://doi.org/10.1016/j.marpetgeo.2004.12.003>.
- Bugge, T., Belderson, R.H., Kenyon, N.H., 1988. The Storegga Slide. *Philos. Trans. R. Soc. Ser. A* 325, 357–388. <https://doi.org/10.1098/rsta.1988.0055>.
- Bull, S., Cartwright, J., Huuse, M., 2009. A subsurface evacuation model for submarine slope failure. *Basin Res.* 21, 433–443. <https://doi.org/10.1111/j.1365-2117.2008.00390.x>.
- Büinz, S., Mienert, J., Berndt, C., 2003. Geological controls on the Storegga gas-hydrate system of the mid-Norwegian continental margin. *Earth Planet. Sci. Lett.* 209, 291–307. [https://doi.org/10.1016/S0012-821X\(03\)00097-9](https://doi.org/10.1016/S0012-821X(03)00097-9).
- Cartwright, J., Santamarina, C., 2015. Seismic characteristics of fluid escape pipes in sedimentary basins: Implications for pipe genesis. *Mar. Pet. Geol.* 65, 126–140. <https://doi.org/10.1016/j.marpetgeo.2015.03.023>.
- Chand, S., Rise, L., Knies, J., Hafliadason, H., Hjelstuen, B.O., Bøe, R., 2011. Stratigraphic development of the south Vøring margin (Mid-Norway) since early Cenozoic time and its influence on subsurface fluid flow. *Mar. Pet. Geol.* 28, 1350–1363. <https://doi.org/10.1016/j.marpetgeo.2011.01.005>.
- Crémière, A., Lepland, A., Chand, S., Sahy, D., Condon, D.J., Noble, S.R., Martma, T., Thorsnes, T., Sauer, S., Brunstad, H., 2016. Timescales of methane seepage on the Norwegian margin following collapse of the Scandinavian Ice Sheet. *Nat. Commun.* 7, 1–10. <https://doi.org/10.1038/ncomms11509>.
- Dalland, A., 1988. A lithostratigraphic scheme for the Mesozoic and Cenozoic succession offshore Norway north of 62° N. *Norw. Petrol. Direct. Bull.* 1–130.
- Davies, R.J., Cartwright, J., 2002. A fossilized Opal A to Opal C/T transformation on the northeast Atlantic margin: support for a significantly elevated palaeogeothermal gradient during the Neogene? *Basin Res.* 14, 467–486. <https://doi.org/10.1046/j.1365-2117.2002.00184.x>.
- Dowdeswell, J.A., Ottesen, D., Rise, L., Craig, J., 2007. Identification and preservation of landforms diagnostic of past ice-sheet activity on continental shelves from three-dimensional seismic evidence. *Geology* 35, 359–362. <https://doi.org/10.1130/G23200A.1>.
- Eidvin, T., Bugge, T., Smelror, M., 2007. The Molo Formation, deposited by coastal progradation on the inner Mid-Norwegian continental shelf, coeval with the Kai Formation to the west and the Utsira Formation in the North Sea. *Nor. J. Geol. Geol. Foren.* 87.
- Eldholm, O., Thiede, J., Taylor, E., 1987. Summary and Preliminary Conclusions. ODP Leg 104. Proc. Ocean Drill. Program, 104 Initial Reports. <https://doi.org/10.2973/odp.proc.ir.104.107.1987>.
- Elger, J., Berndt, C., Rüpke, L., Krastel, S., Gross, F., Geissler, W.H., 2018. Submarine slope failures due to pipe structure formation. *Nat. Commun.* 9, 1–6. <https://doi.org/10.1038/s41467-018-03176-1>.
- Forsberg, C.F., Locat, J., 2005. Mineralogical and microstructural development of the sediments on the Mid-Norwegian margin. *Mar. Pet. Geol.* 22, 109–122. <https://doi.org/10.1016/j.marpetgeo.2004.12.002>.
- Gauer, P., Kvalstad, T.J., Forsberg, C.F., Bryn, P., Berg, K., 2005. The last phase of the Storegga Slide: simulation of retrogressive slidodynamics and comparison with slide-scar morphology. *Mar. Pet. Geol.* 22, 171–178. <https://doi.org/10.1016/j.marpetgeo.2004.10.004>.
- Gay, A., Berndt, C., 2007. Cessation/reactivation of polygonal faulting and effects on fluid flow in the Vøring Basin, Norwegian Margin. *J. Geol. Soc. Lond.* 164, 129–141. <https://doi.org/10.1144/0016-76492005-178>.
- Hafliadason, H., Sejrup, H.P., Nygård, A., Mienert, J., Bryn, P., Lien, R., Forsberg, C.F., Berg, K., Masson, D., 2004. The Storegga Slide: architecture, geometry and slide development. *Mar. Geol.* 213, 201–234. <https://doi.org/10.1016/j.margeo.2004.10.007>.
- GEBCO Compilation Group, 2020. GEBCO 2020 Grid (doi:10.5285/a29c5465-b138-234d-e053-6c86abc040b9).
- Hafliadason, H., Lien, R., Sejrup, H.P., Forsberg, C.F., Bryn, P., 2005. The dating and morphology of the Storegga Slide. *Mar. Pet. Geol.* 22, 123–136. <https://doi.org/10.1016/j.marpetgeo.2004.10.008>.
- Harbitz, C.B., Lovholt, F., Pedersen, G., Masson, D.G., 2006. Mechanisms of tsunami generation by submarine landslides: A short review. *Nor. Geol. Tidsskr.* 86, 255–264.
- Hill, J.C., Driscoll, N.W., Weissel, J.K., Goff, J.A., 2004. Large-scale elongated gas blowouts along the U.S. Atlantic margin. *J. Geophys. Res. Solid Earth* 109, 1–14. <https://doi.org/10.1029/2004JB002969>.
- Hjelstuen, B.O., Eldholm, O., Skogseid, J., 1999. Cenozoic evolution of the northern Vøring margin. *Bull. Geol. Soc. Am.* 111, 1792–1807. [https://doi.org/10.1130/0016-7606\(1999\)111<1792:ceotnv>2.3.co;2](https://doi.org/10.1130/0016-7606(1999)111<1792:ceotnv>2.3.co;2).
- Hjelstuen, B.O., Sejrup, H.P., Hafliadason, H., Nygård, A., Berstad, I.M., Knorr, G., 2004. Late Quaternary seismic stratigraphy and geological development of the south Vøring margin, Norwegian Sea. *Quat. Sci. Rev.* 23, 1847–1865. <https://doi.org/10.1016/j.quascirev.2004.03.005>.
- Hovland, M., Heggland, R., De Vries, M.H., Tjelta, T.I., 2010. Unit-pockmarks and their potential significance for predicting fluid flow. *Mar. Pet. Geol.* 27, 1190–1199. <https://doi.org/10.1016/j.marpetgeo.2010.02.005>.
- Hühnerbach, V., Masson, D.G., 2004. Landslides in the North Atlantic and its adjacent seas: an analysis of their morphology, setting and behaviour. *Mar. Geol.* 213, 343–362. <https://doi.org/10.1016/j.margeo.2004.10.013>.
- Hustoft, S., Mienert, J., Büinz, S., Nouzé, H., 2007. High-resolution 3D-seismic data indicate focussed fluid migration pathways above polygonal fault systems of the mid-Norwegian margin. *Mar. Geol.* 245, 89–106. <https://doi.org/10.1016/j.margeo.2007.07.004>.
- Hustoft, S., Dugan, B., Mienert, J., 2009. Effects of rapid sedimentation on developing the Nyegga pockmark field: constraints from hydrological modeling and 3-D seismic data, offshore mid-Norway. *Geochem. Geophys. Geosyst.* 10 <https://doi.org/10.1029/2009GC002409>.
- Ireland, M.T., Davies, R.J., Goulty, N.R., Carruthers, D., 2011. Structure of a silica diagenetic transformation zone: the Gjallar Ridge, offshore Norway. *Sedimentology* 58, 424–441. <https://doi.org/10.1111/j.1365-3091.2010.01170.x>.
- Jongepier, K., Rui, J.C., Grue, K., 1996. Triassic to early Cretaceous stratigraphic and structural development of the northeastern Møre Basin margin, off Mid-Norway. *Nor. Geol. Tidsskr.* 76, 199–214.

- Kaminski, P., Urlaub, M., Grabe, J., Berndt, C., 2020. Geomechanical behaviour of gassy soils and implications for submarine slope stability: a literature analysis. *Geol. Soc. Spec. Publ.* 500, 277–288. <https://doi.org/10.1144/SP500-2019-149>.
- Karstens, J., Hafliðason, H., Becker, L.W.M., Berndt, C., Rüpke, L., Planke, S., Liebetrau, V., Schmidt, M., Mienert, J., 2018. Glacigenic sedimentation pulses triggered post-glacial gas hydrate dissociation. *Nat. Commun.* 9, 1–11. <https://doi.org/10.1038/s41467-018-03043-z>.
- Kawamura, K., Sasaki, T., Kanamatsu, T., Sakaguchi, A., Ogawa, Y., 2012. Large submarine landslides in the Japan Trench: a new scenario for additional tsunami generation. *Geophys. Res. Lett.* 39, 3–7. <https://doi.org/10.1029/2011GL050661>.
- Kjøberg, S., Schmiedel, T., Planke, S., Svensen, H.H., Millett, J.M., Jerram, D.A., Galland, O., Lecomte, I., Schofield, N., Haug, Ø.T., Helsem, A., 2017. 3D structure and formation of hydrothermal vent complexes at the Paleocene-Eocene transition, the Møre Basin, mid-Norwegian margin. *Interpretation* 5, SK65–SK81. <https://doi.org/10.1190/INT-2016-0159.1>.
- Knaust, D., 2009. Characterisation of a Campanian deep-sea fan system in the Norwegian Sea by means of ichnofabrics. *Mar. Pet. Geol.* 26, 1199–1211. <https://doi.org/10.1016/j.marpetgeo.2008.09.009>.
- Kvalstad, T.J., Andresen, L., Forsberg, C.F., Berg, K., Bryn, P., Wangen, M., 2005. The Storegga Slide: evaluation of triggering sources and slide mechanics. *Mar. Pet. Geol.* 22, 245–256. <https://doi.org/10.1016/B978-0-08-044694-3.50025-1>.
- Laberg, J.S., Baeten, N.J., Lågstad, P., Forwick, M., Vorren, T.O., 2013. Formation of a large submarine crack during the final stage of retrogressive mass wasting on the continental slope offshore northern Norway. *Mar. Geol.* 346, 73–78. <https://doi.org/10.1016/j.margeo.2013.08.008>.
- Lawrence, G.W.M., Cartwright, J.A., 2009. The initiation of sliding on the mid Norway margin in the Møre Basin. *Mar. Geol.* 259, 21–35. <https://doi.org/10.1016/j.margeo.2008.12.006>.
- Lawrence, G.W.M., Cartwright, J.A., 2010. The stratigraphic and geographic distribution of giant craters and remobilised sediment mounds on the mid Norway margin, and their relation to long term fluid flow. *Mar. Pet. Geol.* 27, 733–747. <https://doi.org/10.1016/j.marpetgeo.2009.10.012>.
- Leynaud, D., Mienert, J., Nadim, F., 2004. Slope stability assessment of the Helland Hansen area offshore the mid-Norwegian margin. *Mar. Geol.* 213, 457–480. <https://doi.org/10.1016/j.margeo.2004.10.019>.
- Leynaud, D., Sultan, N., Mienert, J., 2007. The role of sedimentation rate and permeability in the slope stability of the formerly glaciated Norwegian continental margin: the Storegga Slide model. *Landslides* 4, 297–309. <https://doi.org/10.1007/s10346-007-0086-z>.
- Leynaud, D., Mienert, J., Vanneste, M., 2009. Submarine mass movements on glaciated and non-glaciated European continental margins: a review of triggering mechanisms and preconditions to failure. *Mar. Pet. Geol.* 26, 618–632. <https://doi.org/10.1016/j.marpetgeo.2008.02.008>.
- L'Heureux, J.-S., Longva, O., Steiner, A., Hansen, L., Vardy, M.E., Vanneste, M., Hafliðason, H., Brendryen, J., Kvalstad, T.J., Forsberg, C.F., Chand, S., Kopf, A., 2012. Identification of weak layers and their role for the stability of slopes at Finneidfjord, Northern Norway. In: *Submarine Mass Movements and Their Consequences*. Springer Netherlands, Dordrecht, pp. 321–330. https://doi.org/10.1007/978-94-007-2162-3_29.
- L'Heureux, J.S., Vanneste, M., Rise, L., Brendryen, J., Forsberg, C.F., Nadim, F., Longva, O., Chand, S., Kvalstad, T.J., Hafliðason, H., 2013. Stability, mobility and failure mechanism for landslides at the upper continental slope off Vesterålen, Norway. *Mar. Geol.* 346, 192–207. <https://doi.org/10.1016/j.margeo.2013.09.009>.
- Li, W., Alves, T.M., Urlaub, M., Georgiopolou, A., Klauke, I., Wynn, R.B., Gross, F., Meyer, M., Repschläger, J., Berndt, C., Krastel, S., 2017. Morphology, age and sediment dynamics of the upper headwall of the Sahara Slide Complex, Northwest Africa: evidence for a large Late Holocene failure. *Mar. Geol.* 393, 109–123. <https://doi.org/10.1016/j.margeo.2016.11.013>.
- Lien, T., 2005. From rifting to drifting: effects on the development of deep-water hydrocarbon reservoirs in a passive margin setting, Norwegian Sea. *Nor. Geol. Tidsskr.* 85, 319–332.
- Locat, J., Lee, H.J., 2002. Submarine landslides: advances and challenges. *Can. Geotech. J.* 39, 193–212. <https://doi.org/10.1139/t01-089>.
- Micallef, A., Masson, D.G., Berndt, C., Stow, D.A.V., 2007. Morphology and mechanics of submarine spreading: a case study from the Storegga Slide. *J. Geophys. Res. Earth Surf.* 112, 1–21. <https://doi.org/10.1029/2006JF000739>.
- Micallef, A., Masson, D.G., Berndt, C., Stow, D.A.V., 2016. Submarine spreading in the Storegga Slide, Norwegian Sea. *Geol. Soc. Mem.* 46, 411–412. <https://doi.org/10.1144/M46.88>.
- Mienert, J., Vanneste, M., Bünz, S., Andreassen, K., Hafliðason, H., Sejrup, H.P., 2005. Ocean warming and gas hydrate stability on the mid-Norwegian margin at the Storegga Slide. *Mar. Pet. Geol.* 22, 233–244. <https://doi.org/10.1016/j.marpetgeo.2004.10.018>.
- Mienert, J., Vanneste, M., Hafliðason, H., Bünz, S., 2010. Norwegian margin outer shelf cracking: a consequence of climate-induced gas hydrate dissociation? *Int. J. Earth Sci.* 99, 207–225. <https://doi.org/10.1007/s00531-010-0536-z>.
- Montelli, A., Dowdeswell, J.A., Ottesen, D., Johansen, S.E., 2018. 3D seismic evidence of buried iceberglid ploughmarks from the mid-Norwegian continental margin reveals largely persistent North Atlantic Current through the Quaternary. *Mar. Geol.* 399, 66–83. <https://doi.org/10.1016/j.margeo.2017.11.016>.
- Neagu, R.C., Cartwright, J., Davies, R., Jensen, L., 2010. Fossilisation of a silica diagenesis reaction front on the mid-Norwegian margin. *Mar. Pet. Geol.* 27, 2141–2155. <https://doi.org/10.1016/j.marpetgeo.2010.09.003>.
- Newton, A.M.W., Huuse, M., 2017. Late Cenozoic environmental changes along the Norwegian margin. *Mar. Geol.* 393, 216–244. <https://doi.org/10.1016/j.margeo.2017.05.004>.
- Omosanya, K.O., Eruteya, O.E., Siregar, E.S.A., Zieba, K.J., Johansen, S.E., Alves, T.M., Waldmann, N.D., 2018. Three-dimensional (3-D) seismic imaging of conduits and radial faults associated with hydrothermal vent complexes (Vøring Basin, Offshore Norway). *Mar. Geol.* 399, 115–134. <https://doi.org/10.1016/j.margeo.2018.02.007>.
- Omosanya, K.O., Duffaut, K., Alves, T.M., Eruteya, O.E., Johansen, S.E., Waldmann, N., 2022. Giant paleo-seafloor craters and mass wasting associated with magma-induced uplift of the upper crust. *Sci. Rep.* 12, 4392. <https://doi.org/10.1038/s41598-022-08205-0>.
- Pakoksung, K., Suppasri, A., Imamura, F., Athanasius, C., Omang, A., Muhari, A., 2019. Simulation of the submarine landslide Tsunami on 28 September 2018 in Palu Bay, Sulawesi Island, Indonesia, using a two-layer model. *Pure Appl. Geophys.* 176, 3323–3350. <https://doi.org/10.1007/s00024-019-02235-y>.
- Planke, S., Rasmussen, T., Rey, S.S., Myklebust, R., 2005. Seismic characteristics and distribution of volcanic intrusions and hydrothermal vent complexes in the Vøring and Møre basins. In: *Petroleum Geology Conference Proceedings*. Geological Society of London, pp. 833–844. <https://doi.org/10.1144/0060833>.
- Reiche, S., Hjelstuen, B.O., Hafliðason, H., 2011. High-resolution seismic stratigraphy, sedimentary processes and the origin of seabed cracks and pockmarks at Nyegga, mid-Norwegian margin. *Mar. Geol.* 284, 28–39. <https://doi.org/10.1016/j.margeo.2011.03.006>.
- Riis, F., Berg, K., Cartwright, J., Eidvin, T., Hansch, K., 2005. Formation of large, crater-like evacuation structures in ooze sediments in the Norwegian Sea. Possible implications for the development of the Storegga Slide. *Mar. Pet. Geol.* 22, 257–273. <https://doi.org/10.1016/j.marpetgeo.2004.10.023>.
- Rise, L., Ottesen, D., Berg, K., Lundin, E., 2005. Large-scale development of the mid-Norwegian margin during the last 3 million years. *Mar. Pet. Geol.* 22, 33–44. <https://doi.org/10.1016/j.marpetgeo.2004.10.010>.
- Rise, L., Chand, S., Hjelstuen, B.O., Hafliðason, H., Bøe, R., 2010. Late Cenozoic geological development of the south Vøring margin, mid-Norway. *Mar. Pet. Geol.* 27, 1789–1803. <https://doi.org/10.1016/j.marpetgeo.2010.09.001>.
- Roelofs, C., Alves, T.M., Omosanya, K.O., 2021. Reutilisation of hydrothermal vent complexes for focused fluid flow on continental margins (Modgunn Arch, Norwegian Sea). *Basin Res.* 33, 1111–1134. <https://doi.org/10.1111/bre.12507>.
- Romundset, A., Bondevik, S., 2011. Propagation of the Storegga tsunami into ice-free lakes along the southern shores of the Barents Sea. *J. Quat. Sci.* 26, 457–462. <https://doi.org/10.1002/jqs.1511>.
- Rydningen, T.A., Laberg, J.S., Kolstad, V., 2016. Late Cenozoic evolution of high-gradient trough mouth fans and canyons on the glaciated continental margin offshore Troms, northern Norway-Paleoclimatic implications and sediment yield. *Bull. Geol. Soc. Am.* 128, 576–596. <https://doi.org/10.1130/B31302.1>.
- Schulten, I., Mosher, D.C., Krastel, S., Piper, D.J.W., Kienast, M., 2019. Surficial sediment failures due to the 1929 Grand Banks Earthquake, St Pierre Slope. *Geol. Soc. Lond. Spec. Publ.* 477, 583–596. <https://doi.org/10.1144/SP477.25>.
- Shanmugam, G., 2021. Deep-Water Processes and Deposits. *Encycl. Geol.* <https://doi.org/10.1016/b978-0-12-409548-9.12541-2>.
- Skogseid, J., Pedersen, T., Eldholm, O., Larsen, B.T., 1992. Tectonism and magmatism during NE Atlantic continental break-up: the Vøring Margin. *Geol. Soc. Lond. Spec. Publ.* 68, 305–320. <https://doi.org/10.1144/GSL.SP.1992.068.01.19>.
- Solheim, A., Berg, K., Forsberg, C.F., Bryn, P., 2005. The Storegga Slide complex: repetitive large scale sliding with similar cause and development. *Mar. Pet. Geol.* 22, 97–107. <https://doi.org/10.1016/j.marpetgeo.2004.10.013>.
- Song, J., Alves, T.M., Omosanya, K.O., Hales, T.C., Ze, T., 2020. Tectonic evolution of strike-slip zones on continental margins and their impact on the development of submarine landslides (Storegga Slide, northeast Atlantic). *Bull. Geol. Soc. Am.* 132, 2397–2414. <https://doi.org/10.1130/B35421.1>.
- Steward, T., Sivakugan, N., Shukla, S.K., Das, B.M., 2011. Taylor's slope stability charts revisited. *Int. J. Geomech.* 11, 348–352. [https://doi.org/10.1061/\(asce\)gm.1943-5622.0000093](https://doi.org/10.1061/(asce)gm.1943-5622.0000093).
- Sultan, N., Cochonat, P., Foucher, J.P., Mienert, J., 2004. Effect of gas hydrates melting on seafloor slope instability. *Mar. Geol.* 213, 379–401. <https://doi.org/10.1016/j.margeo.2004.10.015>.
- Sun, Q., Wang, W., Shi, F., Alves, T.M., Gao, S., Xie, X., Wu, S., Li, J., 2022. CRUNUP of landslide-generated tsunamis controlled by paleogeography and sea-level change. *Commun. Earth Environ.* 3, 244 (2022). <https://doi.org/10.1038/s43247-022-00572-w>.
- Swiecicki, T., Gibbs, P.B., Farrow, G.E., Coward, M.P., 1998. A tectonostratigraphic framework for the mid-Norwegian region. *Mar. Pet. Geol.* 15, 245–258. [https://doi.org/10.1016/S0264-8172\(97\)00029-9](https://doi.org/10.1016/S0264-8172(97)00029-9).
- Taylor, D.W., 1937. Stability of earth slopes. *J. Bost. Soc. Civ. Eng.* 24, 197–247.
- Terzaghi, K., 1925. *Erdbaumechanik auf bodenphysikalischer Grundlage*. F. Deuticke.
- Trincardi, F., Cattaneo, A., Correggiari, A., Ridente, D., 2004. Evidence of soft sediment deformation, fluid escape, sediment failure and regional weak layers within the late Quaternary mud deposits of the Adriatic Sea. *Mar. Geol.* 213, 91–119. <https://doi.org/10.1016/j.margeo.2004.10.003>.
- Urlaub, M., Geersen, J., Krastel, S., Schwenk, T., 2018. Diatom ooze: crucial for the generation of submarine mega-slides? *Geology* 46, 331–334. <https://doi.org/10.1130/G39892.1>.
- Vogt, P.R., 1997. Hummock fields in the Norway Basin and Eastern Iceland Plateau: Rayleigh-Taylor instabilities? *Geology* 25, 531–534. [https://doi.org/10.1130/0091-7613\(1997\)025<0531:HFITNB>2.3.CO;2](https://doi.org/10.1130/0091-7613(1997)025<0531:HFITNB>2.3.CO;2).
- Xu, W., Germanovich, L.N., 2006. Excess pore pressure resulting from methane hydrate dissociation in marine sediments: a theoretical approach. *J. Geophys. Res. Solid Earth* 111, 1–12. <https://doi.org/10.1029/2004JB003600>.